Hindawi
Geofluids
Volume 2020, Article ID 8868259, 22 pages
https://doi.org/10.1155/2020/8868259

Research Article

Subcritical Phase Separation and Occurrence of Deep-Seated Brines at the NW Caldera Vent Field, Brothers Volcano: Evidence from Fluid Inclusions in Hydrothermal Precipitates

Alexander Diehl,[1,2] **Cornel E. J. de Ronde**,[3] **and Wolfgang Bach**[1,2]

[1]*Department of Geosciences, University of Bremen, Bremen, Germany*
[2]*MARUM Center for Marine Environmental Sciences, Bremen, Germany*
[3]*Department of Earth Resources & Materials, GNS Science, Lower Hutt 5010, New Zealand*

Correspondence should be addressed to Alexander Diehl; diehl@uni-bremen.de

Received 16 April 2020; Revised 26 July 2020; Accepted 12 August 2020; Published 16 September 2020

Academic Editor: Shengnan Nancy Chen

The northwestern caldera wall of Brothers volcano in the southern Kermadec arc features several clusters of hydrothermal venting in a large area that extends from near the caldera floor (~1700 mbsl) almost up to the crater rim (~1300 mbsl). Abundant black smoker-type hydrothermal chimneys and exposed stockwork mineralization in this area provide an excellent archive of hydrothermal processes that form seafloor massive sulfide deposits. Using sulfate precipitates from chimneys and stockwork recently recovered by remotely operated vehicles, we conducted fluid inclusion microthermometry and Sr isotope studies to determine the role of phase separation and mixing between vent fluid and seawater. The variability in the vast majority of fluid inclusion salinities (i.e., 0.1–5.25 wt.% NaCl eq.) and entrapment temperatures of up to 346°C are indicative of phase-separated hydrothermal fluids. Large salinity variations in samples with entrapment temperatures mostly below the boiling temperature for the sample's depth show that the majority of fluids ascending below the NW Caldera are phase separating in the subsurface and cooling, prior to discharge. In several samples, entrapment temperatures of over 343°C suggest that phase-separating fluids have at least sporadically exited the seafloor at the NW Caldera site. Isobaric-isenthalpic mixing trends between coexisting phase-separated vapors and brines with seawater are consistent with phase-separated fluids at near-seafloor pressures of ~170 bar and suggest that the vast majority of the ascending fluids continue to phase separate to within tens to hundreds of meters below seafloor prior to mixing with seawater. A small subset of the most saline fluid inclusions (up to 18.6 wt.% NaCl eq.) is unlikely formed by near-seafloor phase separation and is considered to be produced either by supercritical phase separation or by the contribution of a magmatic brine from near the magmatic-hydrothermal interface. $^{87}Sr/^{86}Sr$ values of sulfate samples range from 0.7049 (i.e., near hydrothermal end-member) to 0.7090 (i.e., near seawater) and show that the crystals grew from vapor- and brine-derived fluids in a hydrothermally dominated mixing regime. Our work provides new insights into mineral growth conditions, mixing regimes, and in particular, the extent and character of subseafloor phase separation during the formation of hydrothermal vents and their underlying stockwork in seawater-dominated, arc-related hydrothermal systems.

1. Introduction

Microthermometric data can be used as geothermobarometers to determine the depth of crystal formation in magmatic-hydrothermal environments, where temperatures are known [1, 2], or to find the temperature of hydrothermal mineralization at known pressure conditions [3, 4]. In seafloor hydrothermal systems, fluid inclusion studies provide information about salinity and temperature of hydrothermal fluids, as well as likely hydrothermal end-member and mixing regimes during mineralization [5–12].

Microthermometric studies on fluid inclusions typically comprise petrographic descriptions and visual observations of phase transitions in the trapped fluids. Measurement of ice-melting temperatures (T_m) and homogenization temperatures (T_h) of two-phase liquid-vapor inclusions enables

calculation of salinity (S_{eq}) and entrapment temperature (T_e) of the inclusions [13, 14]. Under the assumption that a fluid inclusion has not changed in volume or composition since it formed in the host crystal, these measurements represent the conditions of the hydrothermal fluid during precipitation of the crystal [15]. In hydrothermal environments, fluid inclusions can record multiple fluctuations providing a record of conditions during the process of mineralization [5, 9, 16, 17].

In addition, values of $^{87}Sr/^{86}Sr$ for sulfate host minerals provide insight into the mixing regime in hydrothermal environments, as demonstrated for the TAG [18], PACMANUS [19], and the Endeavour Segment [8] hydrothermal systems. The fractionation factor for Sr isotopes during the precipitation of sulfate crystals is neglectable [20], and thus, $^{87}Sr/^{86}Sr$ values in sulfate can be used either as a tracer for Sr in the hydrothermal fluid or as a "fingerprint" of the seawater-fluid mixture the crystal has precipitated from. The combination of fluid inclusion T_e with temperatures deduced from $^{87}Sr/^{86}Sr$ values for fluid-seawater mixing hence may provide evidence for conductive cooling (or conductive heating) and constrain thermobarometric fluid inclusion results [12].

We combined microthermometric data of fluid inclusions with $^{87}Sr/^{86}Sr$ data of sulfate hosts to provide detailed insights into the extent of phase-separation processes and mixing regimes in hydrothermal environments. The mineralization at the NW Caldera (and Upper Caldera) vent site can be regarded to as a modern analogue for volcanogenic massive sulfides. Here, extensive sulfate mineralization occurred simultaneously to sulfide deposition and access to chimneys and their underlying stockwork provide an excellent opportunity to use this approach and investigate phase separation and seawater entrainment related to the deposition of massive sulfides.

2. Geologic Setting

The submarine Brothers volcano is part of the southern Kermadec arc and is situated ~350 km NNE of the North Island of New Zealand (Figure 1). Brothers volcano is arguably one of the most well-studied submarine arc volcanoes in the world. Various studies have focused on its volcanic structure [21, 22] and magmatic evolution [22–26].

The mostly dacitic volcano [22–24, 26, 27] has a 3 × 3.5 km wide caldera that hosts numerous vent sites that have been delineated by shipborne and/or autonomous underwater vehicle plume and magnetic surveys [28–32]. Active hydrothermal venting occurs at three vent sites on the caldera walls (i.e., Upper Caldera, NW Caldera, and West Caldera (not shown), Figure 2(a)) and at two vent sites atop the resurgent cones (i.e., Upper Cone and Lower Cone, Figure 2(a)) in the south-central part of the caldera [28, 29, 33].

The nature and extent of hydrothermal activity and its circulation [28, 31, 34–40] and mineralization [7, 33, 36, 41–43] have been addressed in various studies.

Recently, IODP expedition 376 drilled basement in five sites at Brothers volcano, and the recovered cores reveal new details on hydrothermal mineral zonation and the links between caldera collapse and the evolution of the hydrothermal system(s) [7, 44].

The Upper Cone and Lower Cone vent sites host relatively low-temperature magmatic volatile-dominated, white smoker-type vents, whereas the most vigorous venting at Brothers occurs at the NW and Upper Caldera sites in the form of numerous clusters of black smoker chimney vents expelling high-temperature (to ~320°C) fluids affected by deep-seated seawater-rock reactions [33, 37, 47, 48]. Here, the large NW Caldera site spans an area of at least 200 × 100 m, extending from 1700 meter below sea level (mbsl) near the caldera floor up to a prominent plateau at 1520 mbsl [31]. Above this plateau, the hydrothermal activity continues to the uppermost part of the caldera rim at 1300 mbsl (the Upper Caldera). The two vent fields are characterized by extensive sulfate and sulfide mineralization manifest as chimneys and stockwork zones [6, 33, 41–43] and are coincident with an area depicting a negative magnetic anomaly [29, 34], projected to extend ~1000 meters below seafloor (mbsf).

The mineralization at the NW Caldera vent site is a consequence of vigorous hydrothermal upwelling and represents a striking modern example of fluid flow beneath volcanogenic massive sulfides. Access to active chimneys and their underlying stockwork is unique and makes the NW Caldera wall an exceptional place to study recent processes related to ore formation. The stockwork zone is dominated by clasts of argillic-propyllitic altered volcanics with disseminated pyrite and massive vein networks of either pyrite ± chalcopyrite or anhydrite + barite [47]. Hydrodynamic models suggest the vent field to be controlled by subsurface permeability structures [39, 40]. Investigations of vent fluid composition [33, 47, 48] show salinity variations that point to phase-separation processes at depth.

Fluid inclusions were studied at Brothers before. Measurements of fluid inclusions in subsurface core samples during IODP expedition 376 demonstrated two types of hydrothermal fluids circulating in the subsurface: subcritically phase-separated fluids with salinities of less than 5 wt.% NaCl eq. and hypersaline brines with salinities of ~32-45 wt.% NaCl eq. that formed as exsolution from a silicate melt, or condensed from a high-temperature single-phase fluid at the magmatic-hydrothermal interface [7]. Microthermometric investigations of two seafloor samples dredged from Brothers NW Caldera did not provide conclusive evidence for phase-separation processes. Measurement of ~85 fluid inclusions in two barite-rich samples showed narrow salinity (S_{eq}) ranges of 3.5 ± 0.2 wt.% NaCl eq. and 3.1 ± 0.2 wt.% NaCl eq., with average homogenization temperatures (T_h) of 254 ± 33°C and 257 ± 22°C, respectively [6]. Furthermore, no physical evidence for boiling (e.g., liquid-rich inclusions in close proximity to vapor-rich inclusions) was observed in that microthermometric study. These authors used small deviations from seawater salinity and fluid inclusion gas analyses to suggest that phase separation may have occurred in the subseafloor. The importance of phase separation in the formation of mineralized chimneys and stockwork zones and its role in the formation of this volcanogenic massive sulfide deposit are further evaluated in the present study.

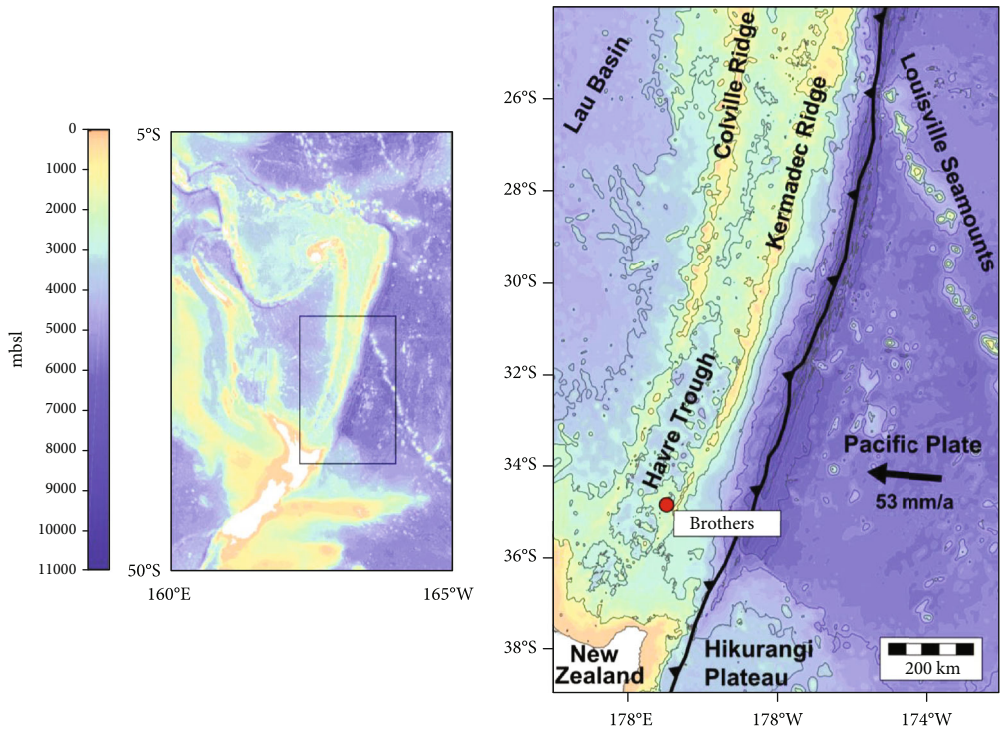

Figure 1: Overview over the South Kermadec arc and location of Brothers volcano. Note: location of subduction zone is given after Bird [45] and the relative plate motion is given after DeMets et al. [46]. Bathymetry data: the GEBCO_2014 Grid, version 20150318, https://www.gebco.net.

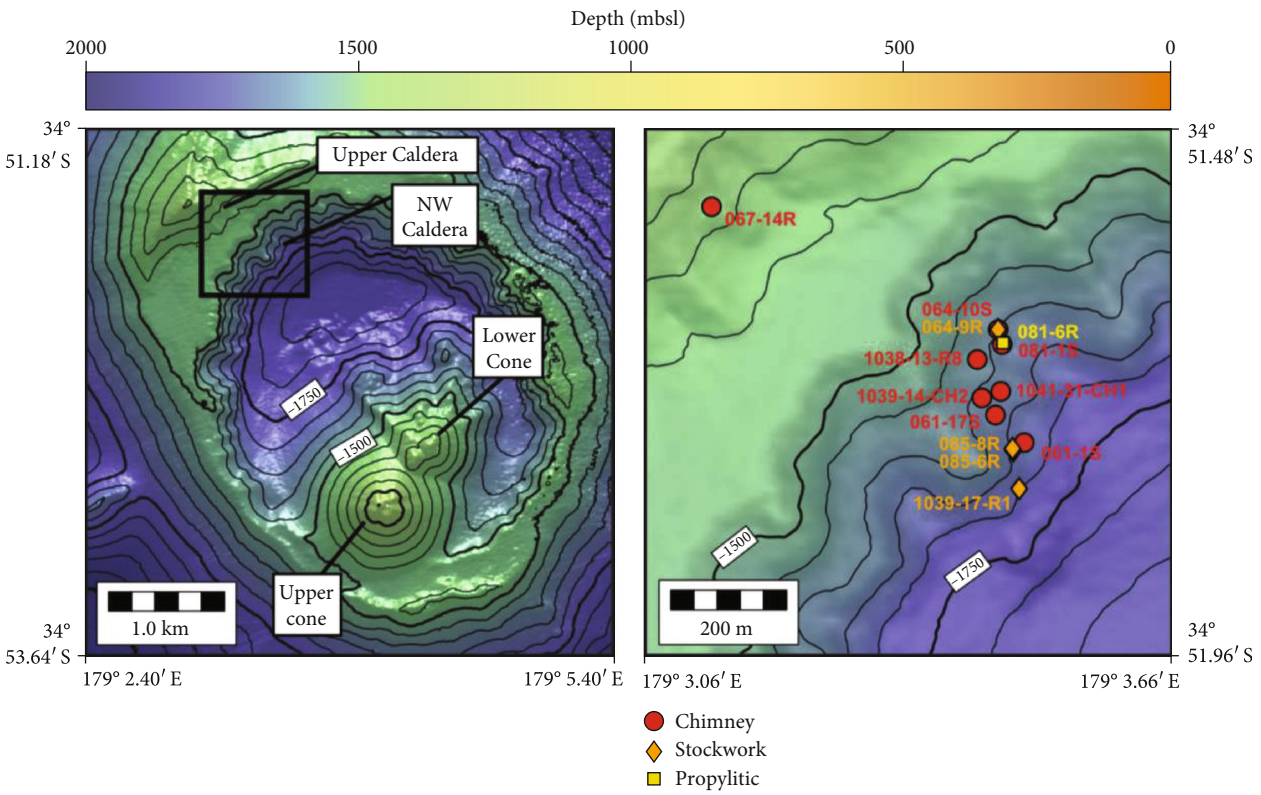

Figure 2: Bathymetry of Brothers caldera. (a) Overview and working areas of both cruises (SO253 and TN350). (b) Sample sites of hydrothermal chimneys, stockwork, and a propyliticly altered rock at the NW Caldera vent site (including one sample from the Upper Caldera). R/V *Sonne* multibeam data from cruise SO253 [51].

Table 1: Sample type, location, and water depth for samples of this study.

Sample name	Sample type	Latitude S	Longitude E	Depth (mbsl)
SO253-061-1S	Chimney	34° 51.7660′	179° 3.4913′	1671
SO253-061-17S	Chimney	34° 51.7409′	179° 3.4586′	1643
SO253-064-9R	Stockwork	34° 51.6634′	179° 3.4617′	1593
SO253-064-10S	Chimney	34° 51.6633′	179° 3.4617′	1593
SO253-067-14R	Chimney	34° 51.5517′	179° 3.1363′	1374
SO253-081-1S	Chimney	34° 51.6768′	179° 3.4662′	1619
SO253-081-6R	Propylitic	34° 51.6755′	179° 3.4671′	1616
SO253-085-6R1	Stockwork	34° 51.7733′	179° 3.4788′	1663
SO253-085-8R	Stockwork	34° 51.7714′	179° 3.4780′	1663
TN350-J2-1038-13-R8	Chimney	34° 51.6905′	179° 3.4380′	1582
TN350-J2-1039-14-CH2	Chimney	34° 51.7254′	179° 3.4433′	1611
TN350-J2-1039-17-R1	Stockwork	34° 51.8078′	179° 3.4855′	1698
TN350-J2-1041-31-CH1	Chimney	34° 51.7195′	179° 3.4646′	1622

3. Methods

3.1. Sample Collection and Preparation. Research expeditions SO253 (R/V *Sonne* and *ROV Quest*, Dec 2016-Jan 2017) and TN350 (R/V *Thompson* and *ROV Jason II*, Mar 2018) set out to investigate hydrothermal activity at Brothers volcano. Both expeditions investigated four of the five active vent sites at Brothers volcano (i.e., NW Caldera, Upper Caldera, Upper Cone, and Lower Cone) using seafloor observations, heat flow measurements, and sampling of hydrothermal fluids and chimneys [49, 50].

The focus of this study is the NW Caldera site and the Upper Caldera site, which are characterized by the regular occurrence of barite and anhydrite in chimneys and stockwork mineralization. Thirteen samples from these sites were collected in order to characterize the nature of the hydrothermal fluids that gave rise to the massive sulfide mineralization (Table 1); twelve samples originate from the lower part of the caldera walls situated below a prominent plateau, or caldera rim, at a water depth of ~1520 mbsl (Figure 2(b); Table 1), and one sample originates from the walls above this plateau in an area referred to as the Upper Caldera. These samples include three distinct lithologies: chimneys, stockwork, and a propylitically altered volcanic wallrock adjacent to the stockwork.

Different structural and mineralogical types of chimneys can be distinguished. A Cu-rich pyrite + chalcopyrite + anhydrite/barite ± sphalerite ± Fe-oxyhydroxide type is most common. These Cu-rich chimneys show a distinct mineralogical zonation with large inner conduits covered by mm-cm thick massive layers of chalcopyrite. This zone rapidly grades into a highly permeable inner wall composed of pyrite + barite + sphalerite. A less permeable, several mm thick outer wall is composed of massive oxyhydroxide crusts. Zn-rich chimneys are mainly composed of pyrite + sphalerite + anhydrite/barite. In some instances, barite or anhydrite occur as a monomineralic layer within these samples. Chimney sample 064-10S represents a third class of Fe-rich chimneys with pyrite + pyrrhotite ± anhydrite ± sphalerite. In contrast to the Cu-rich type, Zn- and Fe-rich chimneys often lack an inner conduit and a strong mineralogical zonation in the chimney wall. Active chimneys of this type often feature fragile beehive tops of finely intergrown anhydrite and sphalerite, through which vent fluid issues diffusely.

The stockwork samples comprise propylitic- to argillic-altered volcanic rocks with disseminated sulfate and sulfide. The rocks are cut by massive veins of sulfate (anhydrite and/or barite) or sulfide (pyrite ± chalcopyrite ± sphalerite). The vein types occur in different areas along the NW Caldera wall, with sulfate veins more prevalent in the northern outcrop of stockwork mineralization (e.g., sample 064-9R). Here, the host rocks are altered to Fe-Mg-rich, mostly chlorite-dominated propylitic assemblages including chlorite + illite + smectite [47]. Sulfide veins are found in the southernmost outcrop (e.g., samples 085-6R, 085-8R, and 1039-17-R1) where the host rocks are altered to an argillic assemblage of quartz + smectite + pyrite + illite [47].

Crystals were extracted from each of these lithologies for detailed microthermometric analyses. In the chimneys, the crystals were extracted either from the central conduit that was lined with barite and/or anhydrite crystals, or from the central wall of the chimney, where mixing of the hot hydrothermal fluids from the inner conduit and ambient seawater has taken place. In the stockwork lithologies, barite and anhydrite crystals either originate from vein material or were extracted from the altered groundmass (in samples with sulfide veins). Finally, crystals from the propylitic-altered volcanic host rock originate from voids that are lined with larger (up to mm size) quartz crystals. Sample preparation for microthermometry consisted of separating transparent minerals from the rock/chimney specimen and picking of euhedral or carefully crushed crystals (with plane crystal or

cleavage faces). The shortest diameter of these crystals was chosen to be smaller than a few hundreds of μm to assure good optical conditions and to prevent thermal gradients within the crystals during microthermometric work. Independent petrographic investigation in thin sections of the corresponding samples has shown that the chimneys typically contain anhydrite, as well as barite. Hence, each individual crystal used for the microthermometric study was investigated under a petrographic microscope, and anhydrite and barite were distinguished by their difference in birefringence (i.e., barite: 0.012; anhydrite: 0.044).

3.2. Fluid Inclusion Petrography and Microthermometry. Our microthermometric study comprised the following: (1) detailed petrographic description and photo documentation of the fluid inclusions, (2) cooling the inclusions to about -60°C with subsequent heating to detect the melting temperature (T_m), and (3) heating to high temperatures to observe the homogenization temperature (T_h) of two-phase inclusions. Petrographic description and photo documentation were followed by the classification of the inclusions as primary, pseudosecondary, or secondary [52, 53]. Additionally, we classified the inclusions according to their phase relations at room temperature.

A Linkam microthermometry heating/freezing stage attached to a Zeiss Axioskop microscope was used to measure T_m and T_h of these fluid inclusions. A Linkam TP92 heat controller provided dynamic temperature control to heat the samples with a defined heating rate between 0.1 and 90°C min^{-1}. An LNP2 flow regulator fed the stage with a constant stream of nitrogen gas from a Dewar of liquid nitrogen. The stage-temperature reading of the system was calibrated using the FLINC® synthetic fluid inclusions in quartz. The freezing point of pure water (0.0°C) and the critical homogenization temperature (374.1°C) were both used to calibrate the stage's thermocouple sensor. During the study, the calibration procedure was repeated 14 times; the freezing point was determined to be 0.04 ± 0.07°C, whereas the critical temperature was determined to be 373.6 ± 0.75°C. This shows that the stage provided accurate temperatures between the measured values of the synthetic fluid inclusions (0 ± 0.1°C; 374 ± 1°C). In each sample, several inclusions were cooled to -100°C to detect the presence of mixtures others than H_2O-NaCl. Since in all but two inclusions no phase transitions except for the ones expected in the H_2O-NaCl system were observed, the H_2O-NaCl system was used to interpret phase transitions. The microthermometric technique to measure T_m and T_h and to calculate salinity (S_{eq}) and entrapment temperature (T_e) using the H_2O-NaCl binary system is described by Bodnar and Vityk [14]. Salinity was calculated directly from T_m, and T_e was calculated from S_{eq} and T_h using a pressure correction and following an isochoric path from the pressure of T_h to the pressure of T_e.

Generally, reequilibration can be a problem in fluid inclusion studies [15]. Considering that the minerals anhydrite and barite have low hardness and are prone to stretching and reequilibration during the fluid inclusion measurement procedure [15], the technique described by Vanko and Bach [54] was applied. That is, their heating and freezing experiments on anhydrite-hosted fluid inclusions showed that during microthermometric measurements, hydration of anhydrite hosts may form gypsum at the inclusion's wall under lower temperature conditions (i.e., at minus several tens °C). In subsequent measurements, the salinity of the fluid inclusion may therefore be increased. This process seems to occur reversibly, as heating the sample to 130°C converts the newly formed gypsum back to anhydrite. Furthermore, Vanko and Bach [54] found that overheating the inclusions by only ~10°C above their T_h commonly leads to stretching or reequilibration and thus significantly changes measured T_h of previously overheated inclusions in anhydrite. Thus, using the procedure proposed by Vanko and Bach [54], inclusions were not measured one after another, but instead, all T_m were measured in freezing runs first. This was an attempt to retain original inclusion shapes (volume) and to prevent stretching. Thereafter, the temperature of the sample was subsequently increased for the T_h measurements with all inclusions observed at 5°C intervals. Following this procedure, no inclusion was significantly overheated before measuring T_h.

3.3. Analysis of $^{87}Sr/^{86}Sr$. Ratios of $^{87}Sr/^{86}Sr$ for five handpicked mineral separates of barite and anhydrite and six bulk sample powders were analyzed by thermal ionization mass spectrometry (TIMS). A Thermo Scientific Triton Plus mass spectrometer was used at the Isotope Geochemistry Laboratory, Center for Marine Environmental Science MARUM, University of Bremen. In total, eleven analyses (eight stockwork, two chimneys, and one propyliticly altered rock) were carried out to determine $^{87}Sr/^{86}Sr$ values on six individual sulfate samples.

The samples were digested in concentrated subboiled HNO_3 at 130°C. Strontium was isolated from the matrix elements, including Ba, using Sr_{Spec} resin by a method adapted from Deniel and Pin [55]. Samples were analyzed with a Ta-emitter on rhenium filaments using the static acquisition method. Two analyses of the NIST SRM 987 reference material were conducted along with the samples, which yielded $^{87}Sr/^{86}Sr$ values of 0.710244 ± 8 and 0.710239 ± 9 that plot well within the long-term reproducibility value of the laboratory (NIST SRM 987 = 0.710249 ± 14; 2σ of $n = 263$). This in turn compares well to average published data for NIST SRM 987 (0.710250 ± 34; 2σ, $n = 1245$, data < 0.7102 and > 0.7103 are discarded; GeoReM database [56], request September 2017).

3.4. Isenthalpic-Isobaric Mixing Models. Fluid inclusion data and $^{87}Sr/^{86}Sr$ ratios were used to develop mixing models between seawater and hydrothermal fluids. We used *T-P* -dependent brine-vapor pairs formed by phase separation to account for the variation in the fluid inclusion data. Potential end-member pairs matching the fluid inclusion data were determined by the phase relations in the H_2O-NaCl system as described by Driesner and Heinrich [57]. Isobaric liquid-vapor (LV) curves were calculated via the program "SOWAT" from which pressure- and temperature-dependent coexisting vapor and brine pairs can be derived.

For simulation of isenthalpic mixing between ambient seawater and phase-separated vapors and brines, we calculated the heat capacity as a function of *T-P-X* following the procedure of Driesner [58]. The thermodynamic properties of pure water are given by Haar et al. [59] and were used to develop a correlation method to calculate the thermodynamic properties of binary H_2O-NaCl solutions. From this data, we calculated the compositional dependency of the heat capacity of salty solutions (see Driesner [58] and references therein). For individual mixing paths of our different end-member brines and vapors with seawater, we simultaneously calculated heat capacities and temperatures of those mixtures.

4. Results

4.1. Fluid Inclusion Petrography and Classification. We studied a total of 471 fluid inclusions hosted by barite ($n = 278$, 59%), anhydrite ($n = 173$, 37%), and quartz ($n = 20$, 4%). The inclusions were measured in chimneys ($n = 237$, 50%), stockwork material ($n = 214$, 46%), and propylitically altered wallrock ($n = 20$, 4%). We separated both barite and anhydrite from chimneys and stockwork zones, while quartz represented vug infills in the one altered rock specimen. All inclusions were classified following the petrographic classification scheme outlined by Roedder [53]. He described primary inclusions to occur as single inclusions, as small groups of inclusions, or in trails that follow crystal growth faces. Secondary inclusions occur as trails parallel to cleavage faces or with no visible relation to crystal growth faces and do intersect crystal boundaries. Pseudosecondary inclusions occur like secondary inclusions, but trails do not intersect crystal boundaries. In our investigation inclusions are classified into primary ($n = 401$; 85%) and secondary ($n = 70$; 15%) inclusions. No pseudosecondary inclusions are identified. Inclusions are either euhedral, with a negative crystal shape ($n = 281$; 59%), round ($n = 115$; 25%), or irregular ($n = 81$; 16%) in shape. Inclusions where the largest diameter is equal to, or larger by three times the smallest diameter, are classified as elongated ($n = 132$; 28%). All shapes occur for primary, as well as secondary, inclusions, but secondary inclusions tend to be rather round. Fluid inclusion size is calculated using the smallest and the largest diameter to calculate the area of an ellipse. Inclusions ($n = 132$; 28%) with an area smaller than $5\,\mu m^2$ are considered small. If the area ranges between 5 and $50\,\mu m^2$, the inclusions are considered medium sized ($n = 227$; 49%), and the remaining inclusions ($n = 105$; 23%) with a size $> 50\,\mu m^2$ are considered large.

The volume proportions of the vapor and liquid phase were estimated from the area expression of the phases in microscopic view. The area occupied by the vapor bubble was related to the total inclusion area. The majority of inclusions are liquid rich at room temperature, with most inclusions ($n = 214$; 46%) having a vapor fraction of 20%. In total, in 402 inclusions (87%), the vapor fraction occupies <50%, while in a smaller number of inclusions ($n = 41$), the vapor fraction occupies ≥50%. The remaining inclusions decrepitated before the liquid-vapor ratio was detected or were found as single-phase (liquid) inclusions. According to phase relations at room temperature, the fluid inclusions are further divided into three types. *Type I* inclusions are single phase and were not further investigated. Abundant ($n = 462$) *Type II* inclusions are two phased and contain a vapor bubble and a liquid phase. *Type II* inclusions are subdivided into liquid-rich *Type IIa* ($n = 418$, 89%) and vapor-rich *Type IIb* ($n = 44$), with a division set at a liquid-to-vapor ratio of 0.5. *Type IIa* and *Type IIb* inclusions both co-occur in single trails. Rare *Type III* inclusions ($n = 9$, 2%) are three-phased and contain a liquid, a vapor bubble, and a transparent solid phase. Figure 3 provides a representative overview of the petrographic relationship of the NW Caldera fluid inclusions.

4.2. Microthermometry. Microthermometric measurements are shown in Table 2 and Figure 4, including T_m of 429 and T_h of 346 inclusions (Figures 4(a) and 4(b)) out of 471 investigated inclusions. Notably, the T_m of two inclusions is +1.8°C and +3.3°C, respectively, which is higher than the T_m for pure H_2O, and hence higher than possible T_m for H_2O-NaCl binary solutions. The melting temperature in these inclusions can only be explained with the presence of solutes that shift T_m towards higher temperatures in these inclusions. Two inclusions have T_m of -14.0°C and -15.0°C, which are distinctly lower than T_m in all other inclusions and result in significantly higher salinities for these inclusions. For the sake of clarity and to keep statistical integrity in our assessment, these four inclusions are excluded in the following figures and tables and will be discussed separately. For 325 inclusions, both T_m and T_h were measured (Figure 4(c), Table 2). For these inclusions, the corresponding S_{eq} and T_e are calculated. As the pressure during homogenization of the fluid inclusions is close to the pressure of entrapment (i.e., the pressure at the seafloor), the path along the isochore is short, and hence, the correction for temperature is similarly small. Overall, the temperature correction (i.e., the difference between T_e and T_h) is small, ranging between 2°C and 10°C (average 9°C).

The inability of being able to detect ice melting in 42 inclusions can be mostly attributed to optical limitations. For example, some *Type II* inclusions were clearly visible, but ice melting was still not observed. As these inclusions are vapor rich, they contain only a small liquid component, which made it hard to observe the process of ice melting. Some of the 134 inclusions, in which T_h could not be determined, were simply missed during heating runs and thus have been excluded to avoid measurements of potentially stretched inclusions. Some inclusions did stretch, or decrepitate, and changed from two phases to a single phase during the microthermometric measurements, even at relatively low temperatures (<<100°C). Indeed, most of the inclusions could not be measured as a consequence of (audible) decrepitation events, which occurred in barite as well as anhydrite during measurement of T_h. Such decrepitation events occurred regularly at temperatures ≥ 300°C. Forty-five inclusions were not measured due to decrepitation events. For all these inclusions, T_h is >270°C; for 39 of them, T_h is >300°C; for 9, T_h is >340°C; for 5 inclusions, T_h is >400°C; and for 2 inclusions, T_h is >500°C. Decrepitation often occurred while

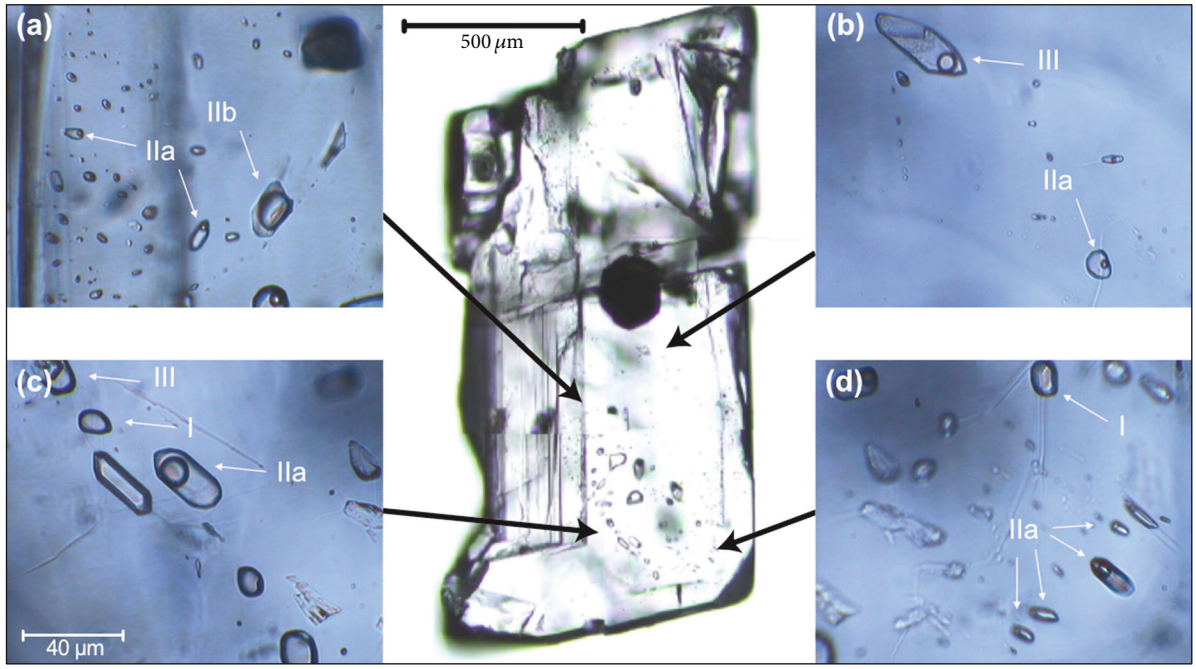

Figure 3: Petrographic relationships for fluid inclusions in sample SO253-085-6R. The photographs were taken at room temperature and show different sizes, shapes, and types of inclusions. (a) Typical *Type IIa* liquid-rich inclusions with a single *Type IIb* vapor-rich inclusion in a primary trail; (b) small group of primary inclusions with *Type IIa* (lower right-hand corner) and a *Type III* daughter-mineral-bearing inclusion (upper left-hand corner); (c, d) two photographs of a prominent primary fluid inclusion trail following crystal growth faces with *Type I-Type III* inclusions and varying LV ratios.

heating *Type IIb* inclusions, which are therefore underrepresented in the statistical treatment of the fluid inclusion data.

In summary, among all inclusions that could not be homogenized, two-third is of *Type IIa* and one-third is of *Type IIb*. The difference to the overall abundance of inclusion types, in which *Type IIb* comprised only 9%, suggests that these inclusions commonly homogenize at higher temperatures and are prone to stretching and/or are prone to decrepitation. For these inclusions, it was noted that the vapor phase grows during heating, instead of shrinking like *Type IIa*. Thus, we suggest that a number of these inclusions homogenize into the vapor phase and represent low-density inclusions.

In *Type III* inclusions, no phase transitions were detected. For two of these inclusions, temperatures of up to 400°C during the microthermometric measurements did not lead to dissolution of the daughter mineral. The fact that no visible phase transition occurred at low temperatures suggests that these inclusions do not contain saline solutions with salinities below the eutectic composition comparable to the measured *Type II* inclusions. If the transparent daughter mineral is a sulfate crystal, these inclusions should show ice melting comparable to *Type II* inclusions. In contrast, if the *Type III* inclusions contain H_2O-NaCl solutions with a salinity above the eutectic composition, no ice melting is to be expected at low T (below 0°C), as we observed. For high-salinity inclusions, the dissolution of halite is the first phase transition to be observed at high temperature, followed by complete homogenization at even higher temperatures. Assuming that the inclusions indeed represent highly saline inclusions with halite daughter minerals and their dissolution occurs above 400°C, this means that the incorporated fluids contain S_{eq} > 40 wt.% NaCl equivalent.

4.3. Salinities and Entrapment Temperatures. A total of 325 inclusions have both T_m and T_h measurements, for which the corresponding S_{eq} and T_e are calculated (Table 2). In addition, S_{eq} values are calculated for 427 inclusions based on thermodynamic relationships in the binary H_2O-NaCl system. Two inclusions with S_{eq} of 17.7 and 18.6 wt.% NaCl eq., respectively, are discussed separately because these two inclusions would impede data visualization and significantly bias statistical parameters.

Calculated salinities (S_{eq}) in the remaining 425 measured fluid inclusions range from 0.1 to almost 9 wt.% NaCl eq., with a mean value of 3.1 ± 1.3 wt.% NaCl eq. (cf. seawater is 3.2 wt.% NaCl equivalent). The S_{eq} data show a multimodal distribution, with two pronounced modes. The first and most prominent group includes 225 inclusions and occurs between 3.0 and 4.0 wt.% NaCl eq. (Figure 5(a)), coincident with salinities in fluid inclusions measured by de Ronde et al. [6]. The second group includes 45 fluid inclusions in a narrower range, between 1.5 and 1.8 wt.% NaCl equivalent. Finally, a number of fluid inclusions show either very low values of S_{eq} of 0–1 wt.% NaCl eq. ($n = 29$) or much higher values of >4 wt.% NaCl eq. ($n = 25$). These fluid inclusions, with noticeably higher and lower salinities when compared to seawater, have not been previously reported in seafloor samples collected from the NW Caldera site. The S_{eq} of *Type*

Table 2: Statistical parameter for individual samples, host minerals, and lithologies in the microthermometric study. Note: two inclusions with extraordinary low T_m (-14.0°C and -15.0°C) as well as two inclusions with T_m higher than that of pure water (+1.8°C and +3.3°C) are excluded. The exclusion of the two highly saline inclusions results in two inclusion less for the sum of S_{eq} than mentioned in the text above.

Sample/lithology/host mineral	N (number of observations)				S_{eq} (wt.% NaCl)					T_e (°C)				
	T_m	S_{eq}	T_{hom}	T_e	Mean	SD	Min	Max	Median	Mean	SD	Min	Max	Median
Chimneys	**216**	**214**	**195**	**181**	**3.2**	**1.2**	**0.2**	**8.5**	**3.4**	**260**	**44**	**135**	**344**	**268**
061-17S	26	24	15	13	3.6	1.3	0.8	8.5	3.6	205	51	149	295	182
061-1S	35	34	34	31	3.6	0.9	0.2	5.2	3.8	246	37	135	335	243
064-10S	34	34	34	31	1.8	1.6	0.2	5.3	0.8	289	32	251	344	269
067-14R	15	15	16	13	3.6	0.6	2.1	5.0	3.4	301	15	277	344	302
081-1S	37	36	34	32	3.6	0.4	3.0	4.4	3.6	246	33	185	303	234
1038-13-R8	39	39	35	35	3.7	1.0	3.3	7.9	3.4	295	4	288	306	296
1039-14-CH2	21	21	19	18	3.6	0.3	3.3	4.4	3.4	226	42	144	298	225
1041-31-CH1	10	10	8	8	3.3	0.5	2.3	3.9	3.4	214	36	169	270	222
Anhydrite (all chimneys)	123	122	117	110	3.1	1.3	0.2	7.9	3.4	279	35	170	344	292
Barite (all chimneys)	93	92	78	71	3.6	0.9	0.2	8.5	3.6	231	42	135	335	234
Stockwork	**195**	**195**	**134**	**127**	**2.9**	**1.3**	**0.1**	**8.9**	**2.6**	**242**	**42**	**155**	**345**	**246**
064-9R	44	44	25	25	2.9	0.9	1.5	4.1	3.0	284	44	184	345	290
085-6R	61	61	42	41	1.9	0.5	0.1	3.9	1.8	241	27	155	295	251
085-8R	33	33	29	25	3.3	1.5	0.9	8.9	3.3	208	28	168	265	198
1039-17-R1	57	57	38	36	3.6	1.4	0.1	8.0	3.4	226	40	155	318	241
Anhydrite (all stockwork)	40	40	26	26	2.4	0.7	1.5	4.1	2.3	257	39	184	331	248
Barite (all stockwork)	155	155	109	101	3.0	1.4	0.1	8.9	3.1	238	42	155	345	245
Propylitic	**17**	**17**	**17**	**17**	**3.5**	**1.1**	**1.1**	**5.0**	**3.6**	**329**	**9**	**306**	**346**	**329**
081-6R	17	17	17	17	3.5	1.1	1.1	5.0	3.6	329	9	306	346	329
Quartz (all propylitic)	17	17	17	17	3.5	1.1	1.1	5.0	3.6	329	9	306	346	329
All	***429***	***425***	***346***	***325***	***3.1***	***1.3***	***0.1***	***8.9***	***3.4***	***257***	***47***	***135***	***346***	***255***
Barite (all samples)	249	246	186	172	3.2	1.3	0.1	8.9	3.4	235	42	135	345	239
Anhydrite (all samples)	163	162	143	136	2.9	1.2	0.2	7.9	3.3	275	37	169	344	289
Quartz (all samples)	17	17	17	17	3.5	1.1	1.1	5.0	3.6	329	9	306	346	329

IIb inclusions essentially show the same data distribution as *Type IIa* inclusions (Figure 5(b)), despite the fact that the relative abundance of inclusions with $S_{eq} > 4$ wt.% NaCl eq. is larger than that for *Type IIa* inclusions. In terms of seawater salinity (S_{SW}), the inclusions are divided into three groups: (1) those with salinities significantly below that of seawater (<3.1 wt.% NaCl eq.), comprising of 33% of the inclusions; (2) salinities of seawater composition (3.1–3.3 wt.% NaCl eq.), comprising of 16% of the inclusions; and (3) salinities significantly higher than seawater (>3.3 wt.% NaCl eq.), comprising 51% of the inclusions. We compared the range in salinities of the fluid inclusions with the salinity variations of the vent fluids from the NW Caldera site (Figure 5(c)). The majority of vent fluid salinities (45%) are seawater like (3.1–3.3 wt.% NaCl eq.) or slightly above (>3.3 wt.% NaCl eq. and up to 4.5 wt.% NaCl eq.) seawater salinity (51%). Only two out of 49 vent fluid salinities (or 4% of the data) lie significantly below the salinity of seawater. While overall the bulk of the vent fluid salinities are similar to those found associated with the fluid inclusions, the most extreme values of $S_{eq} < 1.7$ wt.% NaCl eq. and $S_{eq} > 4.5$ wt.% NaCl eq. that represent a considerable fraction (20% of all measured S_{eq}) of the fluid inclusion data are not seen in vent fluid compositions.

T_e for the entire set of inclusions fall in the range between 135°C and 347°C, with a mean value of 257 ± 47°C. This value is remarkably close to fluid inclusion results given in the study of de Ronde et al. [6]. The distribution of T_e, like S_{eq}, also shows a multimodal distribution with two pronounced modes (Figure 5(d)). One mode is situated at around 250°C and coincides with the average T_h from the work of de Ronde et al. [6]. Another one consists of inclusions with T_e of 280–300°C, which overlaps with the interval of highest T_h given by de Ronde et al. [6]. A third mode at T_e of 330°C shows temperatures in excess of the aforementioned study, with the exception of one inclusion with T_h of 322°C in de Ronde et al. [6]. The few T_e determinations made for *Type IIb* inclusions (Figure 5(e)) show that the relative abundance of inclusions formed at temperatures in excess of 325°C (seven out of 18, or > 33% of all *Type IIb* T_e determinations) is higher than that for *Type IIa* inclusions, coincident with a higher proportion of relatively high S_{eq}

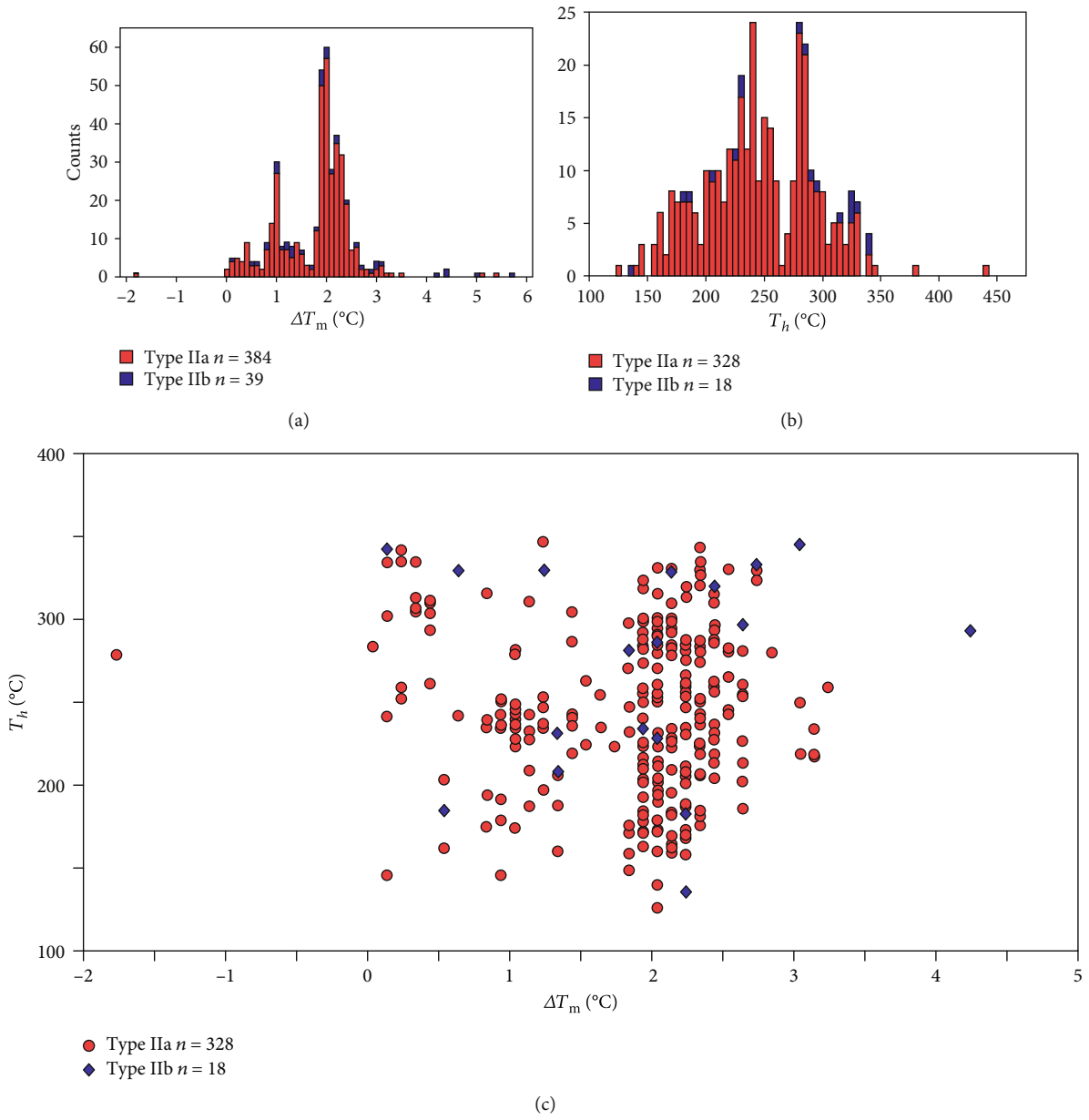

Figure 4: Microthermometric raw data plotted by inclusion types. *Type IIa* inclusions are shown in red, and *Type IIb* inclusions shown in blue. (a) Histogram of measured ice-melting temperatures expressed as the melting point depression (ΔT_m). (b) Histogram of homogenization temperature (T_h). (c) ΔT_m vs. T_h for inclusions where both parameters are determined.

inclusions. Measured vent fluid temperatures (Figure 5(f)) agree with T_e values for the fluid inclusions. Temperatures of a small number of vent fluids are below 250°C, but most samples sit in two groups of higher fluid temperatures. The first group comprises of about 30% of all data with fluid temperatures between 250 and 275°C and can be matched to the T_e mode at ~250°C. The second group (43%) is given by fluid temperatures of between 290 and 310°C and can be matched to the inclusion T_e mode at 300°C. One fluid sample with a temperature of 320°C can be matched to the inclusion mode of higher T_e at 330°C. Higher vent fluid temperatures of $T > 325$°C have not been reported although such high fluid inclusion T_e represents almost 10% of all measured T_e.

4.4. Temperature and Salinity Variations with Lithology and Depth. If we consider the different lithologies (chimneys, stockwork, and propylitic wallrock), we find that each lithology and each mineral type records the entire spectrum of fluid inclusion S_{eq} and T_e (Figure 6), especially inclusions with salinities similar to, or greater than, seawater that mark the most pronounced mode of the entire population are found in stockwork, chimneys, and propylitic rock. Still, there are apparent relationships between S_{eq}/T_e and lithology, as well as mineral type. These are the lowest S_{eq} (<0.7 wt.% NaCl eq.) and T_e of 280–320°C which are measured almost exclusively in chimney samples (Figures 6(a) and 6(b)). In terms of host minerals in chimneys, a

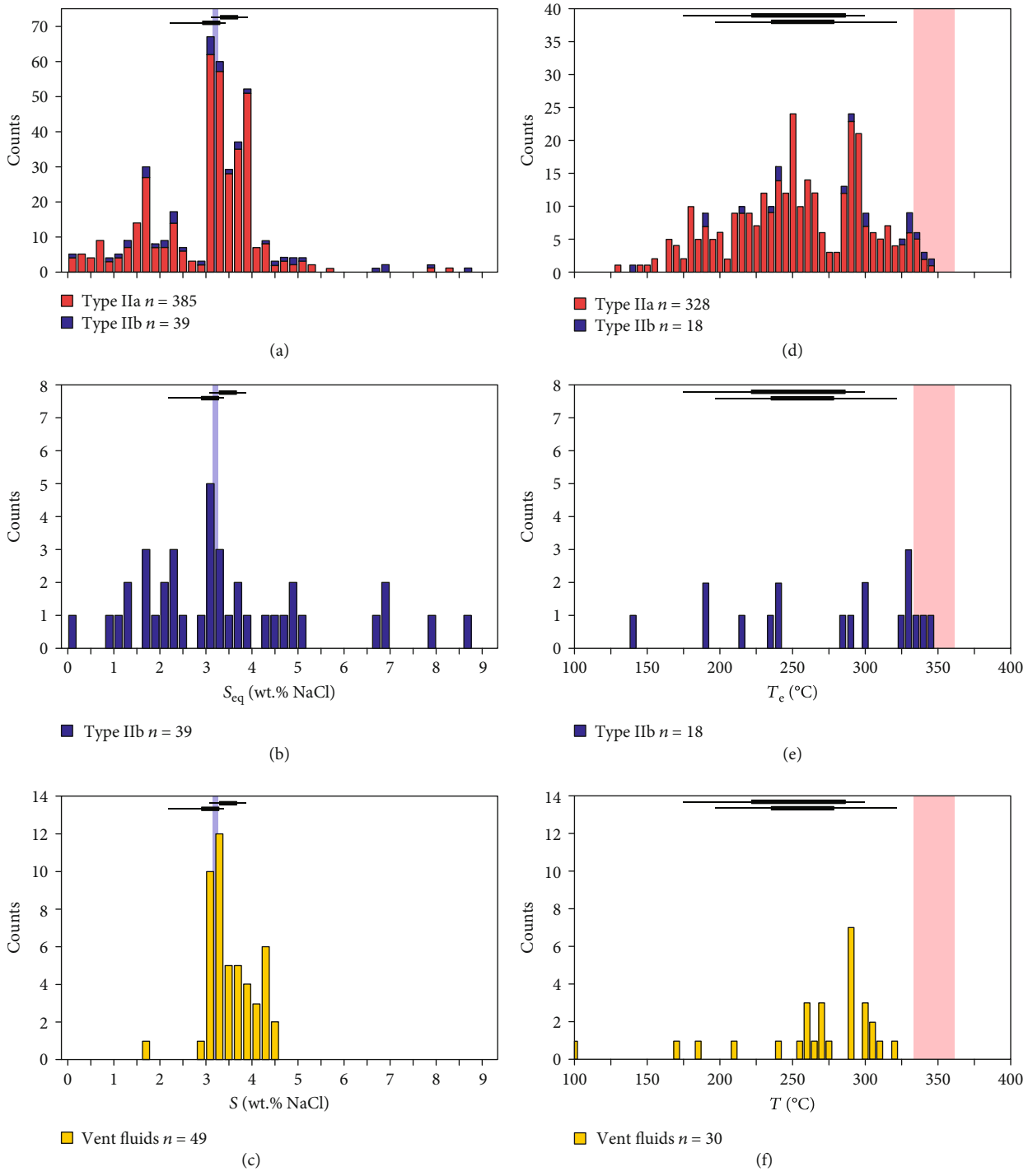

Figure 5: Fluid inclusion salinities (S_{eq}) and entrapment temperatures (T_e) in comparison with vent fluid salinities and temperatures. (a) Histogram of S_{eq} and T_e for all inclusions. The results are color coded according to inclusion types. *Type IIa* inclusions are shown in red, and *Type IIb* inclusions shown in blue. (b) S_{eq} for *Type IIb* inclusions. (c) Salinities in vent fluid samples [33, 47, 48]. (d) Histogram of T_e for all inclusions. (e) Histogram of T_e for *Type IIb* inclusions. (f) Temperatures of vent fluid samples [33, 47, 48]. Note: the vertical blue line denotes seawater salinity (S_{sw}). The red-shaded area marks the boiling temperatures at seafloor pressure (from the base of caldera floor at 1850 mbsl to the uppermost part of the caldera rim at 1300 mbsl). The black horizontal lines give the range (thin lines) and the mean values ± standard deviations (thick lines) of S_{eq} and T_h of two barite samples investigated in the fluid inclusion study by de Ronde et al. [6].

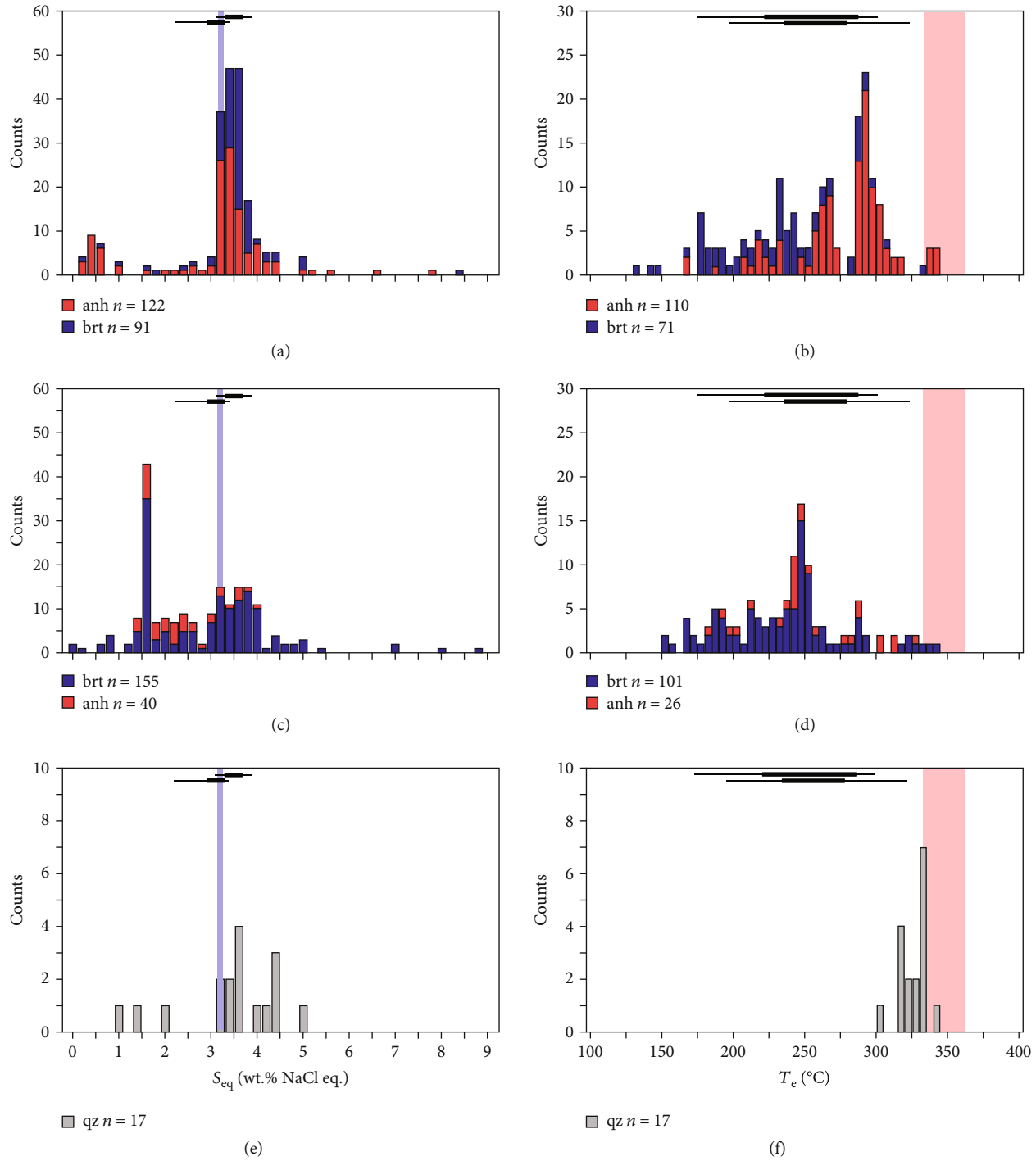

FIGURE 6: Histograms of salinities (S_{eq}) and entrapment temperatures (T_e) plotted by lithology and host minerals. (a, b) Histograms of S_{eq} and T_e for fluid inclusions from chimneys. (c, d) Histograms of S_{eq} and T_e for inclusions from stockwork mineralization. (e, f) Inclusions from open vugs in propyliticly altered wallrock adjacent to the stockwork veins. The inclusions are color coded after their host mineral; anh: anhydrite in red; brt: barite in blue; qz: quartz in grey. Explanation of black bars is given in Figure 5.

relationship between inclusion composition and the host mineral is found. Fluid inclusions in anhydrite record proportionally lower salinity fluids and higher temperatures when compared to barite-hosted fluid inclusions (Figures 6(a) and 6(b)).

In contrast to chimneys, low-salinity inclusions in stockwork samples are mostly confined to higher S_{eq}, in the range of 0.7–3.0 wt.% NaCl eq., and are predominantly found at lower T_e of ~250°C (Figures 6(c) and 6(d)). In terms of mineral types, there is no apparent relationship between S_{eq}/T_e

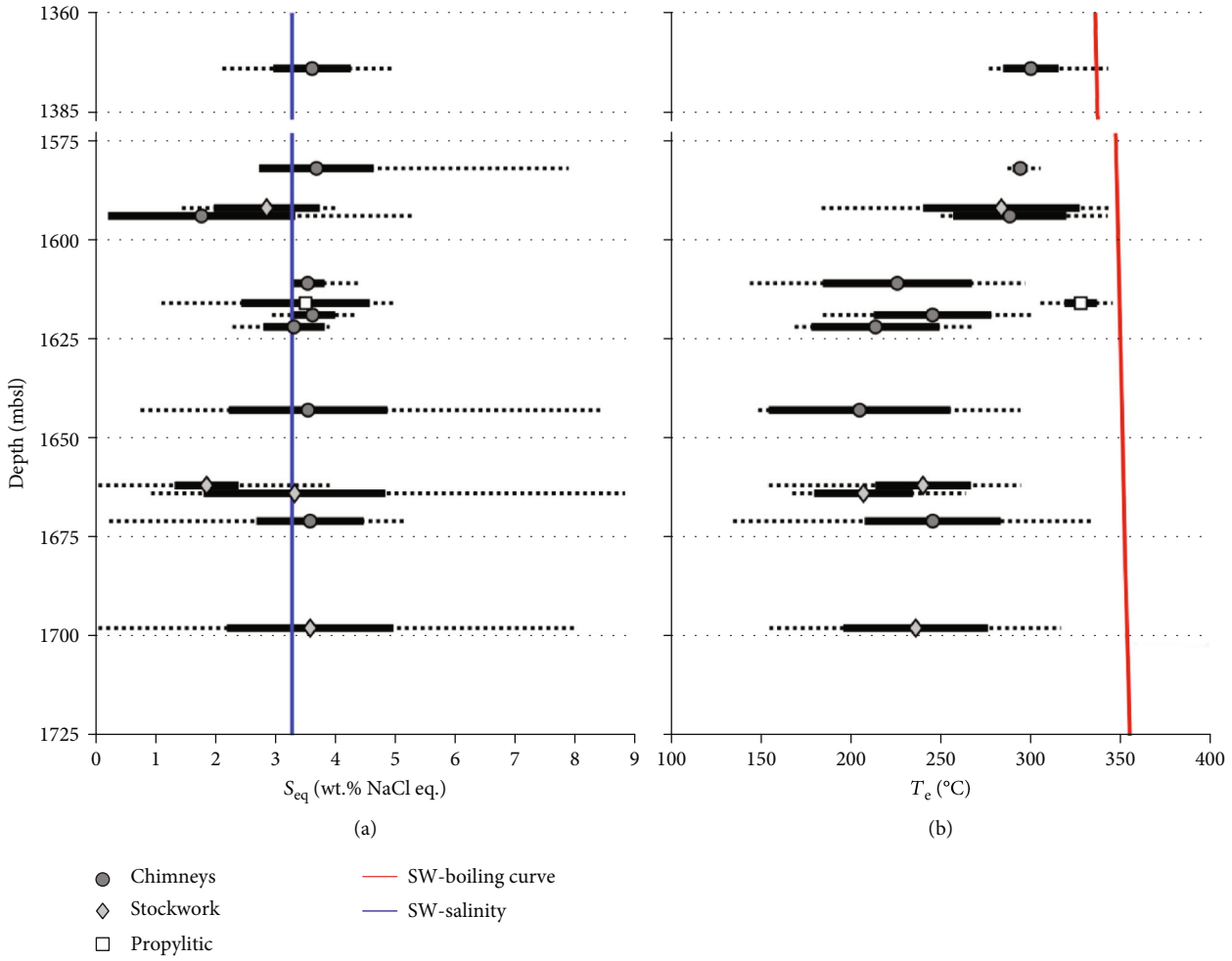

FIGURE 7: Variation of fluid inclusion data (T_e and S_{eq}) for different samples with respect to depth. Symbols represent sample mean values, thick black lines represent the mean ± standard deviation of a sample, and the dashed lines represent the range to minimum and maximum values. (a) S_{eq} compared to seawater salinity (blue line). (b) T_e compared to the depth-to-boiling-point curve for seawater (red line; calculated after Driesner and Heinrich [57] and assuming a seawater density of 1030 kg m^{-3}). Note samples with identical depths were slightly shifted to make the data visible (i.e., 1593 mbsl and 1664 mbsl). Also note the break in depth scale in the *y*-axis which enables the detail of each sample to be seen over the entire depth range.

and the host mineral for stockwork mineralization (Figures 6(c) and 6(d)). Anhydrite and barite inclusions cover virtually the entire range of S_{eq}/T_e. However, inclusions with the lowest (<1 wt.% NaCl eq.) and highest (>4 wt.% NaCl eq.) salinities are here exclusively found in barite crystals.

Inclusions from quartz crystals in the propylitically altered wallrock (Table 2, Figures 6(e) and 6(f)) show a narrower but still broad range of S_{eq} (1.1–5.0 wt.% NaCl eq.) and a narrow range of higher T_e (306–346°C). Despite the small sample size of only 17 measured inclusions, these fluid inclusions make up almost half of the inclusions in the mode of highest T_e (~330°C) given for the overall dataset.

The variation of T_e and S_{eq} as a function of water depth is shown in Figure 7. The fluid inclusion data is plotted on a projected depth profile of the inner caldera at Brothers and is compared to seawater salinity and the seawater boiling curve. This plot shows how the modes of S_{eq} and T_e in the overall dataset are related to individual samples (cf. Table 2).

The mean salinities for single samples range from 1.8 ± 1.6 (sample 064-10S) to 3.7 ± 1.0 wt.% NaCl eq. (sample 1038-R8), with medians of 0.9 and 3.4 wt.% NaCl eq., respectively. Mean T_e values for single samples range from 208 ± 28°C (i.e., sample 085-8R) to 329 ± 9°C (i.e., sample 081-6R). Median values for these samples are 198°C and 329°C, respectively.

Mean values for S_{eq} close to seawater are characteristic of 11 of 13 samples (Figure 7(a)). Two samples give mean S_{eq} < 2 wt.% NaCl equivalent. Although mean S_{eq} are similar to seawater on average, individual inclusions in 10 of 13 samples contain a wide range of S_{eq} (>>3 wt.% NaCl eq.) spanning almost the entire range of the dataset. Four samples contain inclusions with very low S_{eq} (<0.5 wt.% NaCl eq.), and in another four samples, inclusions with the highest S_{eq}

Table 3: $^{87}Sr/^{86}Sr$ values of mineral separates used in conjunction with fluid inclusion studies and adjacent bulk rock from stockwork samples. brt: barite; anh: anhydrite.

Sample name	Sample type	Inclusion separates		Bulk samples
		brt	anh	brt/anh
064-9R	Stockwork	0.709040 ± 7		
064-9R	Stockwork		0.705260 ± 10	
064-9R	Stockwork			0.708572 ± 5
064-9R	Stockwork			0.707551 ± 5
067-14R	Chimney		0.706807 ± 8	
081-6R	Propylitic			0.706130 ± 6
085-6R1	Stockwork		0.704852 ± 14	
085-6R1	Stockwork			0.706894 ± 6
085-6R1	Stockwork			0.706848 ± 8
085-8R	Stockwork			0.706365 ± 6
1038-13-R8	Chimney		0.705921 ± 5	

> 8 wt.% NaCl eq. are found. By contrast, three samples are different with a small range of S_{eq} in individual inclusions (1039-CH2, 081-1S, and 1041-CH1 at 1611, 1619, and 1622 mbsl, respectively). In these samples, the mean S_{eq} of all inclusions is close to seawater and the range of S_{eq} (<<2 wt.% NaCl eq.) is comparably small, which is expressed by a small standard deviation (<0.6 wt.% NaCl eq.). The S_{eq} distribution in these three samples is most comparable to the inclusion data of de Ronde et al. [6].

Mean T_e in individual samples cluster into three groups (Figure 7(b)). Eight of 13 samples with a mean T_e of 200–250°C are situated deeper than 1600 mbsl. Four samples with a distinctly higher mean T_e of 280–300°C are situated shallower than 1600 mbsl. The T_e mean value of 330°C for the propylitically altered wallrock is significantly higher than all other mean temperatures. In all fluid inclusion samples, the mean T_e is lower than the depth-to-boiling-point temperature of seawater for any given depth. However, a subset of samples shows maximum T_e very close to (i.e., within 5°C) the boiling point curve for seawater. Such high T_e occur in four of 13 samples investigated (i.e., samples 061-17S, 064-10S, 064-9R, and 081-6R; cf. Table 2).

4.5. $^{87}Sr/^{86}Sr$ Composition of Mineral Separates and Bulk Samples. Values for $^{87}Sr/^{86}Sr$ for eleven mineral separates and bulk rock samples range from near hydrothermal end-member values established for NW Caldera vent site hydrothermal fluids (0.70437 ± 0.00015, $n = 10$, composition extrapolated to Mg = 0) to near seawater values (0.70918; [47]) (Table 3; Figure 8). The least radiogenic sample is an anhydrite separate from sample 085-6R1 with an $^{87}Sr/^{86}Sr$ value of 0.704852. By contrast, the most radiogenic sample is a barite separate from sample 064-9R with an $^{87}Sr/^{86}Sr$ value of 0.709040. The $^{87}Sr/^{86}Sr$ value for two samples (064-9R and 085-6R1) has been measured multiple times in bulk rock samples and inclusion separates. The measurements show that the isotopic composition for these samples is highly variable. For example, in sample 064-9R, the

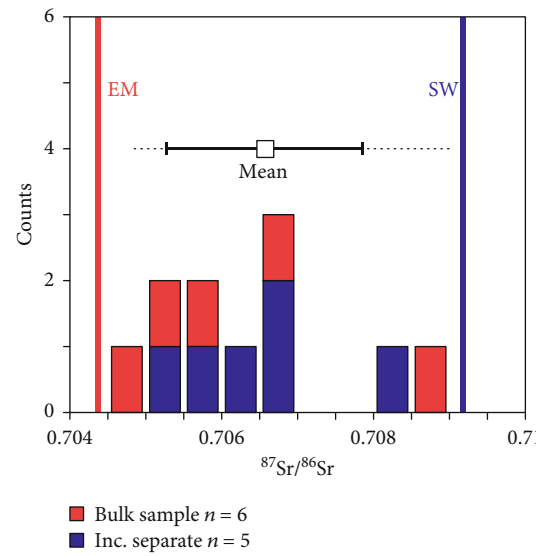

Figure 8: Histogram of $^{87}Sr/^{86}Sr$ values of mineral separates and adjacent bulk samples from stockwork and chimney samples. The red and blue vertical lines show the $^{87}Sr/^{86}Sr$ of hydrothermal end-member (EM) and seawater (SW) after Diehl [47]. The horizontal lines show the mean value ± SD (thick black line) and the minimum to maximum value (dotted line) measured in 11 samples.

$^{87}Sr/^{86}Sr$ values vary from 0.705260 to 0.708572 in four subsamples of one rock specimen. Similarly, for sample 085-6R1, values of four subsamples of one specimen range from 0.704852 to 0.706894. This shows the inhomogeneous nature of the sulfate crystals originating in this environment. Values of $^{87}Sr/^{86}Sr$ have been measured either from single crystals from inclusion separates or from small portions of crushed bulk rock adjacent to the inclusion samples. The measurement of six crushed bulk samples shows a narrower range of isotope compositions from 0.706130 to 0.708572 than the larger range of 0.704852 to 0.709040 for individual crystals (cf. Table 3 and Figure 8).

Table 4: Characteristics of coexisting hydrothermal end-member vapor-brine pairs used in our best-fit isenthalpic mixing model. Temperature, pressure, and salinities ($S_{Em,Vapor}$, $S_{Em,Brine}$ in wt.% NaCl eq.) were derived from the L+V surface of the H_2O-NaCl system [57]. F_{Vapor} and F_{Brine} (mass fractions in the corresponding vapor and brine pairs) were calculated by the lever rule and by assuming a source fluid with seawater salinity. The Sr concentrations (mmol kg^{-1}) of the vapor-brine pairs were calculated by assuming Sr partitioning behavior identical to that of salt and using a seawater Sr concentration of 0.09 mmol kg^{-1}; the $^{87}Sr/^{86}Sr$ value of 0.7044 (0.70437 ± 15) for the hydrothermal end-member was derived from 10 hydrothermal fluid samples by back calculating to Mg = 0 mmol kg^{-1} [47].

Mixing model	T_{EM} (°C)	P bar	$^{87}Sr/^{86}Sr_{EM}$	F_{Vapor} (wt.%)	$S_{EM,Vapor}$ (wt.% NaCl eq.)	$Sr_{EM,Vapor}$ (mmol kg^{-1})	F_{Brine} (wt.%)	$S_{EM,Brine}$ (wt.% NaCl eq.)	$Sr_{EM,Brine}$ (wt.%)
1	354	170	0.70440	31	0.009	0.00025	69	5.25	0.1477
2	425	340	0.70440	77	1.55	0.0436	23	8.65	0.2432

4.6. Isenthalpic-Isobaric Mixing Models. The fluid inclusion and $^{87}Sr/^{86}Sr$ data from this study are used to develop mixing models between seawater and hydrothermal fluids. The fluid inclusion data given in this work provide direct evidence for phase separation having occurred at the NW Caldera site, as other recent studies do [7, 33, 48].

In simulations of isenthalpic mixing between ambient seawater, phase-separated vapors, and brines, we calculate the heat capacity as a function of *T*-*P*-*X* following the procedure of [58]. Isenthalpic-isobaric mixing models are then employed to examine possible mixing trends for generating the observed variability in T_e and S_{eq} in fluid inclusions, as well as Sr isotope variations in the host phases. In these models, we determine the positions of phase-separated end-member fluids and their corresponding mixing trends in *T*-*X* space, where *T* is temperature and *X* is either salinity or Sr isotope composition. The computations are conducted for subcritical conditions, based on evidence from the fluid inclusion data that demonstrate T_e near the boiling temperature at seafloor pressures and S_{eq} close to 0 wt.% NaCl equivalent. Further, we compute simulations for supercritical conditions to account for high-salinity inclusions (>>5 wt.% NaCl eq.). Isobaric *T*-*X* sections of phase relations in *P*-*T*-*X* space are computed following Driesner and Heinrich [57]. Our model results predict the consequences of mixing between subcritically and supercritically phase-separated fluids and seawater in terms of S_{eq}, T_e, and $^{87}Sr/^{86}Sr$ variations along isenthalpic-isobaric mixing paths. Plausible brine-vapor pairs are tabulated in Table 4.

Hydrothermal end-member fluids produced by near-seafloor phase- separation at 170 bar (~1700 mbsl or ~0–300 mbsf; dependent on the location on the caldera wall) and by subseafloor phase separation at supercritical pressures of 340 bar (~3000 mbsl or ~1300–1600 mbsf assuming a fully hydrostatic pressure regime) are considered. We compute mixing paths between these phase-separated end-member fluids with ambient seawater (5°C).

Figure 9 presents our best-fit isenthalpic mixtures at a pressure of 170 bar with an end-member temperature of 354°C. The vapor-brine phases are formed when a fluid with seawater salinity fractionates into 31 wt.% vapor ($S_{EM,vapor}$ = 0.0009 wt.% NaCl eq.) and 69 wt.% brine ($S_{EM,brine}$ = 5.25 wt.% NaCl equivalent). Phase separation of an ascending fluid terminates under equilibrium conditions at 170 bar. The vapor and brine fractions of the chosen end-member broadly resemble the overall occurrence of fluid inclusion salinities with approximately 33% of all inclusions showing S_{eq} lower than seawater, and 51% of inclusions showing S_{eq} higher than seawater (the remaining inclusions are indistinguishable from seawater salinity). Phase segregation of this brine/vapor pair can produce any composition between those two end-members, and subsequent mixing with seawater results in the *T*-*X* space highlighted in Figure 9(a).

The model scenario may explain the vast majority of fluid inclusion data except for two groups of inclusions. The first group involves those inclusions with lowest S_{eq} in combination with low T_e. These inclusions can be explained only when significant conductive cooling (of ~50–100°C) is involved in addition to the hydrothermal fluid/seawater mixing. The second group comprises inclusions with relatively high salinities (S_{eq} > 4.8 wt.% NaCl eq.) in combination with low T_e (<270°C). A number of these inclusions (i.e., those with S_{eq} < 5.25) can also be explained by conductive cooling, but the model cannot account for the even higher salinities with the chosen end-member brine/vapor pair. A lower T_m was measured in a number of inclusions where no T_h could be determined. These inclusions are not plotted in Figure 9(a) but provide direct evidence for a contribution of fluids with significantly higher salinities than the range explained by this model. In total, the T_m of nine inclusions indicate S_{eq} higher than 6 wt.% NaCl eq. and up to 18.6 wt.% NaCl equivalent.

Figures 9(b) and 9(c) show how formation temperatures and salinities covary with the $^{87}Sr/^{86}Sr$ ratios for the mixed fluids. The mixing models can reasonably account for the variation of inclusion T_e with respect to Sr isotope values (Figure 9(b)) and explain the covariation of salinity and $^{87}Sr/^{86}Sr$ (Figure 9(c)). Extremely low salinities in vapor end-members are expected to be accompanied by extremely low Sr concentrations (as the partitioning behavior of Sr is assumed to be equal; cf. Table 4). Vapor end-member hydrothermal fluids that mix with seawater will therefore exhibit seawater-like isotopic signatures, even with small seawater fractions in the mix.

Mixing models involving phase separation at different pressures are applied to account for the fluid inclusion data. Applying higher pressures in the phase-separation process results in both the temperature of the brine-vapor pair, as well as the salinity of the vapor end-member increasing.

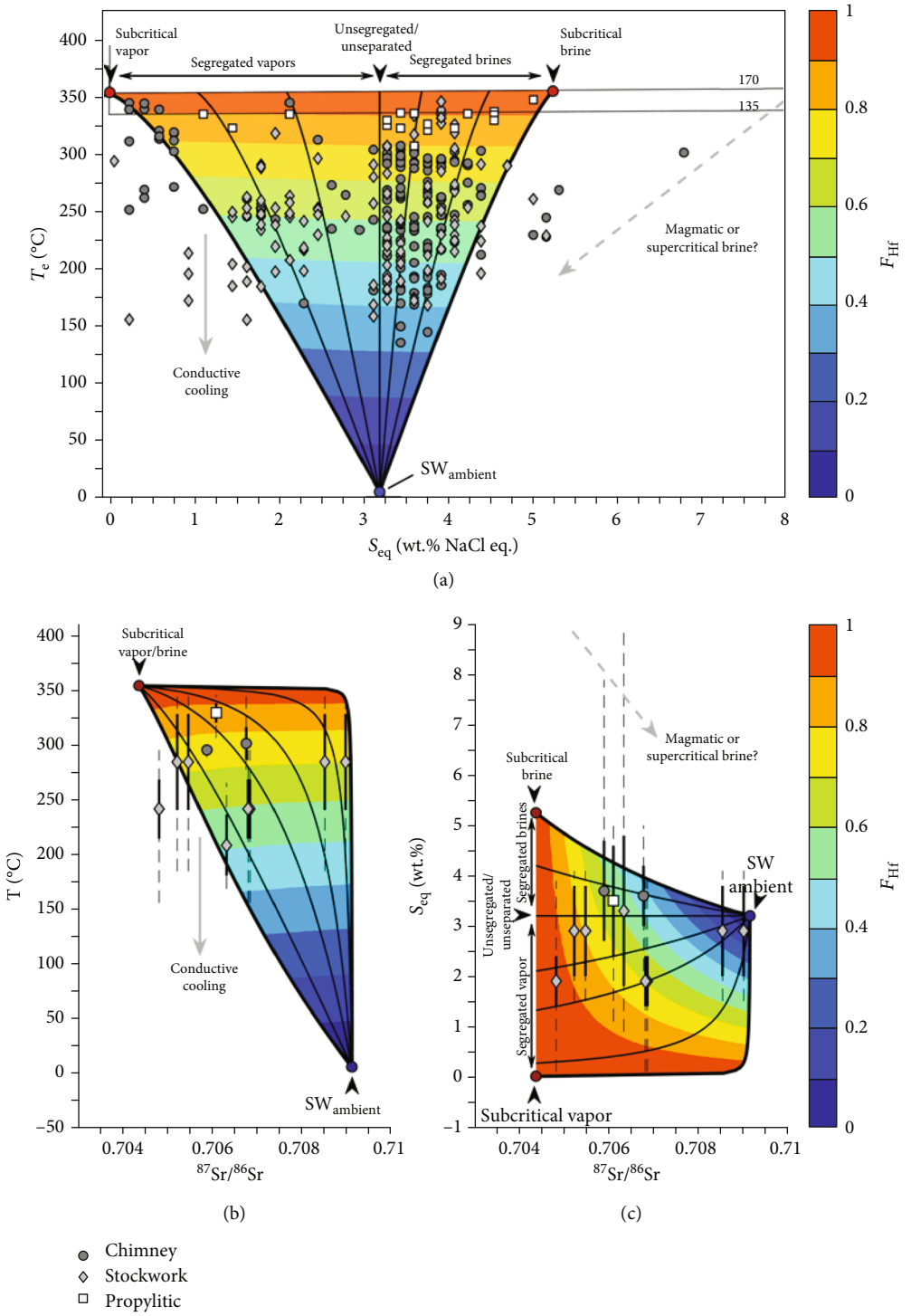

FIGURE 9: Mixing model 1. (a) Salinity-temperature relation for isenthalpic mixing paths of mixtures between phase-separated hydrothermal fluids and ambient seawater at 170 bar. Thin black horizontal curves represent isobaric V+L curves at 135 and 170 bar (calculated after Driesner and Heinrich [57]). The thick black curves denote isenthalpic mixing of the chosen brine-vapor pair. The thin lines represent fluids derived from phase segregation of the phase-separated brine and vapor. The color code gives the mass fraction of the hydrothermal fluid F_{Hf} in the mix (i.e., $F_{Hf} = 1$ pure hydrothermal fluid to $F_{Hf} = 0$ pure seawater). (b) Relationship between temperature and $^{87}Sr/^{86}Sr$ for mixing model 1. Vertical lines represent the natural variability of inclusion data in S_{eq} and T_e (dashed lines: min to max, thick lines: mean ± SD). Note how low-saline high-temperature fluids can precipitate sulfate with near seawater $^{87}Sr/^{86}Sr$. (c) Relationship between salinity and $^{87}/^{86}Sr$ for the mixing model.

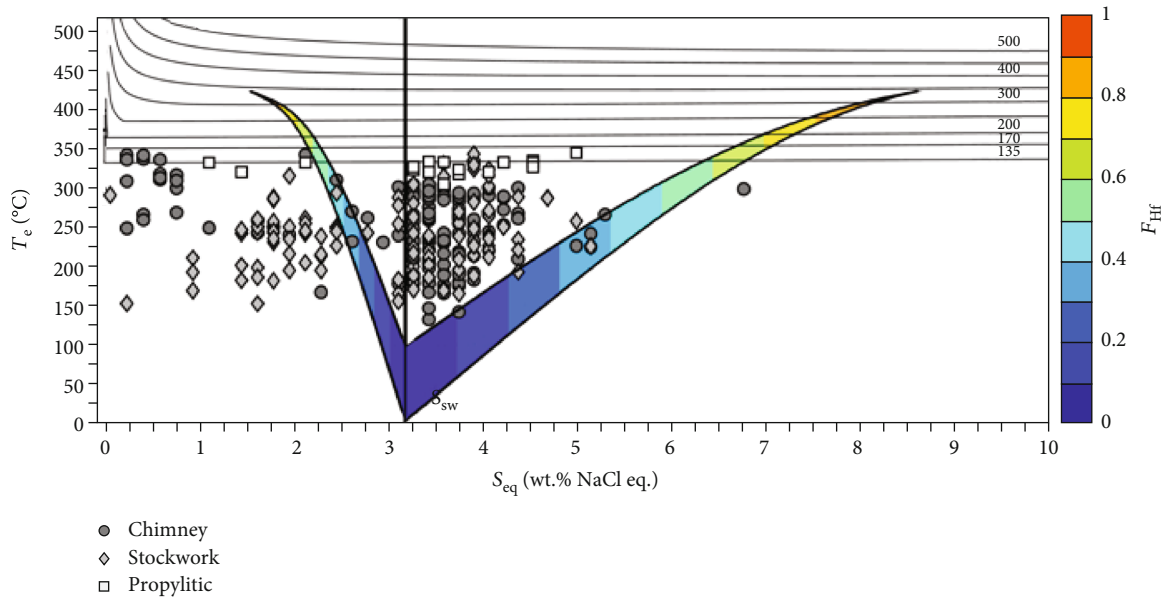

Figure 10: Mixing model 2. Salinity-temperature relation for isenthalpic mixing paths of mixtures between a supercritically phase-separated hydrothermal fluid and ambient to heated seawater at 340 bar. High-salinity inclusions fall on this mixing trend.

These models can therefore not account for the observed variability found in the fluid inclusion data, except if extreme conductive cooling scenarios are invoked.

Moreover, the occurrence of high S_{eq} fluid inclusions is not likely explained by shallow (near-seafloor) phase separation, because formation of a brine with much higher salinities (i.e., >10 wt.% NaCl) would require fractionation of large amounts of vapor from the original fluid and would lead to a vapor/brine fractionation where the vapor fraction dominates.

The high-salinity inclusions, however, can be explained by scenarios involving supercritical phase separation. We calculate an isobaric-isenthalpic mixing line for a vapor/brine pair of supercritically phase-separated fluids at a pressure of 340 bar (Table 4). The high-salinity inclusions plot well along a mixing trend between seawater and a phase-separated brine at such a pressure (Figure 10). The scarcity of data due to the lack of T_h measurements for these high-salinity inclusions and the broad and indefinite freedom to choose pressure, temperature, and fractionation between a supercritical vapor and brine do not allow us to constrain the depth or nature of this possible supercritical phase-separation process any further.

5. Discussion

5.1. Evidence for Phase Separation from Microthermometry. The vast majority (98%) of fluid inclusions associated with mineralization at the Brothers NW Caldera (including the Upper Caldera) hydrothermal vent field show S_{eq} between 0.1 and 5.25 wt.% NaCl equivalent. Most of these inclusions are two phased, liquid-rich at room temperature, and are classified as *Type IIa*, while a significant number of these inclusions (48%) fall in a range between 3.3 and 5.25 wt.% NaCl equivalent. This group of inclusions coincides with previously measured vent fluid compositions [33, 47, 48] and previous fluid inclusion studies of seafloor samples by de Ronde et al. [6]. The latter reported a mean S_{eq} of 3.2 ± 0.3 wt.% NaCl eq. and a mean T_h of 256 ± 27°C, which are almost identical to the results given in this study (i.e., S_{eq} of 3.1 ± 1.3 wt.% NaCl eq.; T_e of 257 ± 47°C; cf. Table 3). However, the ranges in both S_{eq} and T_h of fluid inclusions indicated by de Ronde et al. [6] are much narrower than that in our study. The authors found that <15% of their inclusions significantly deviated from seawater S_{eq} and suggest that their data shows a slight increase of S_{eq} with increasing T_h. Based on their microthermometric results from two samples and from gas analyses of fluid inclusions in those same samples, de Ronde et al. [6] suggest that the fluid inclusion data indicate subseafloor phase separation of the hydrothermal fluid prior to mixing with seawater and subsequent venting. Our microthermometric data, representing a much larger sample size, are consistent with the results of de Ronde et al. [6] and reinforce the significant role phase separation plays in the hydrothermal vent field of the NW and Upper Caldera, which accounts for the vast majority of fluid inclusions.

In our microthermometric dataset, about 50% of all inclusions have trapped hydrothermal fluids with S_{eq} greater than seawater. Similarly, about 33% of the measured inclusions have trapped hydrothermal fluids with S_{eq} less than seawater. Only about 16% of all inclusions can be regarded to have seawater salinity. By assuming that this distribution is representative for the hydrothermal regime in a temporal and spatial fashion, we conclude that the hydrothermal fluids that passed through the NW Caldera site are dominantly brine-derived solutions, with a significant fraction comprising vapor-derived solutions, and only a subordinate fraction with seawater-derived fluids that may not have undergone any phase separation.

A significant number of inclusions (14%) had $S_{eq} < 1.7$ wt.% NaCl eq., with S_{eq} as low as 0.1 wt.% NaCl equivalent. The occurrence of these inclusions provides direct evidence for shallow phase separation in depths of tens to few hundreds meter below seafloor and the circulation of vapor-rich hydrothermal fluids that are barely diluted by seawater. The occurrence of such low-salinity vapor-derived fluids is reported for the first time in seafloor samples from the NW Caldera vent field.

In a small subset (2%) of all inclusions, salinities > 5.25 wt.% NaCl eq. and up to 18.6 wt.% NaCl eq. were observed. These high-salinity inclusions are abundant in *Type IIb* and are similarly reported for the first time in seafloor samples from the NW Caldera vent field. Highly saline brines (32–45 wt.% NaCl eq.) in fluid inclusions have recently been reported in a microthermometric study of drillcore samples from the NW Caldera and the Cone Sites at Brothers [7]. Additional evidence for the occurrence of high-salinity fluids in our seafloor samples eventually was found in some rare fluid inclusions with transparent daughter crystals. The three-phased inclusions did not show any phase transitions up to 400°C. The tendency of decrepitation events during the microthermometric investigations has prevented us from heating to higher temperatures and evaluating the phase relations at such high temperatures. If the solid phase in these inclusions represents halite, these inclusions must contain fluids with $S_{eq} > 40$ wt.% NaCl eq., as dissolution of halite would occur below temperatures of 400°C for inclusions with lower salinities. We assume that the measured salinities ($S_{eq} > 5.25$) and the three-phased inclusions provide a direct link between the saline brines in the drillcore samples and attest the sporadic occurrence of these brines in the shallow part of the hydrothermal system and at the seafloor.

The entrapment temperatures in this study range between 135 and 347°C with three pronounced modes found regarding fluid inclusion T_e; the first and second modes fall between 230–270°C and 290–310°C, respectively. These two modes are in accordance with vent fluid temperatures in the NW Caldera site [33, 47, 48] and the microthermometric fluid inclusion study of de Ronde et al. [6]. In addition, we found fluid inclusions in a less pronounced (10% of all inclusions) third mode, with temperatures of 320–346°C that occur in all mineralization types and host mineral phases, and which have higher temperatures than measured for vent fluids in the NW Caldera. Maximum T_e in several samples plot very close to the depth-to-boiling-point curve of seawater for the corresponding seafloor pressure. In addition to high T_e and extreme S_{eq} variations, we find petrographic evidence for phase separation. Inclusions with variable liquid-vapor ratios occur in single trails of fluid inclusions with similar T_h. Such inclusions are consistent with entrapment from phase-separated fluids [4].

The proposed occurrence of subcritical phase separation at the NW Caldera vent field is not unique and has been mentioned by several authors [6, 7, 31, 33, 47, 48]. Phase separation was predicted by numerical simulations of fluid and heat transport for Brothers volcano by Gruen et al. [39] and Gruen et al. [40]. Though, our study presents a wider range of fluid salinities and a larger population of non-seawater salinities compared to previous investigations of vent fluids and fluid inclusions in seafloor samples. This indicates that phase separation plays a larger role in controlling fluid compositions and modulating metal transport to the seafloor than previously appreciated.

5.2. Extent and Depth of Phase Separation in the NW Caldera Wall Vent Field. Analyzing the fluid inclusions in individual samples shows that maximum T_e in four of 13 samples are very close to the depth-to-boiling-point temperature at the corresponding seafloor pressure. This observation suggests that in the recent past, actively phase-separating fluids have sporadically reached the seafloor without much cooling, or mixing, in the subseafloor, and that the minerals have grown from phase-separating fluids. This process has not been observed by direct vent fluid temperature measurements during the two expeditions to the NW Caldera site in 2016/2017 and 2018, where samples for this study were recovered. All measured vent fluid temperatures, both previously published and those of the two recent cruises, were notably (by ≥15–20°C) below the boiling point of seawater at the corresponding seafloor pressures [33, 47, 48].

Fluid salinities are variable in ten out of 13 samples, ranging from ≤50% to ≥150% seawater salinity, and are consistent with phase-separation processes having occurred prior to sulfate mineral growth. Salinity is a good marker of phase separation as fluid inclusions with a large range in S_{eq} and correspondingly T_e below the boiling temperature represent mixing of hot, upwelling fluids and entrained ambient seawater prior to crystal growth. Such mixing processes cease phase separation in the subsurface due to efficient cooling but preserve variations in S_{eq}. This is consistent with the considerable variability of vent fluid salinities in combination with vent fluid temperatures explicitly lower than the boiling temperature. We therefore suggest that phase separation is a ubiquitous feature in the NW Caldera hydrothermal system, but the amount of cooling and mixing with cold seawater en route to the seafloor is variable in space and time.

An important observation made in this study is that fluid inclusions in the majority of samples and even within single crystals have trapped almost the entire spectrum of S_{eq} (i.e., less than and greater than seawater) observed at the NW Caldera vent site as a whole. This suggests that not only the process of fluid-seawater mixing but also the process of phase separation itself is indeed highly variable in space and time. Time-series analyses of vent fluid compositions at MOR hydrothermal systems showed a temporal evolution of phase-separation processes in vent sites. For example, vent sites at the Juan de Fuca ridge and EPR 9°50′ N were visited following magmatic events and were found to be predominantly discharging vapor phase-derived fluids [60–62]. Fluids at the same sites then transitioned into seawater- or brine-derived solutions after some months to years after these magmatic events had occurred.

Generally, for the NW Caldera site, radiometric dating of barite mineralization has shown that mineralization has occurred over an extended period of time, with ^{226}Ra/Ba ages

for (sulfate-rich) mineralization of ~1200 years and evidence for even older hydrothermal activity to exceed 15,000 years [31, 63, 64]. For active chimneys, $^{228}Th/^{228}Ra$ and/or $^{228}Ra/^{226}Ra$ ages have shown that recent mineralization has predominantly occurred over the last four years with some chimneys dating back to 30–40 years, at time of sampling [31, 33]. Since barite and anhydrite analyzed in this study are often intergrown and have probably precipitated coevally, we tentatively transfer the radiometric results to this study. A timespan of several years to tens of years is sufficient for several magmatic events, including intrusions of magmatic dikes in the deep subsurface, to affect the hydrothermal system by providing additional heat and lead to an alternating entrapment of brine- and vapor-derived fluids in our sulfate-hosted fluid inclusions.

Detailed dating has shown that typically the age of mineralization along a transect of active chimneys progressively increases from the outer wall to the inner wall, if not younger chimneys have grown adjacent to older ones [33]. If the phase-separation process was controlled by magmatic events and a progression from vapor- to brine-dominated fluids at the NW Caldera site occurred, we expect that certain salinity ranges are restricted to some samples depending on the timing of growth of the individual host crystal. However, the salinities are widely distributed throughout most of the discrete samples. This requires a rather ephemeral feature controlling the occurrence of vapors and brines. We suggest that the key in this variability is the process of phase-segregation, as proposed by Butterfield et al. [65]. Phase segregation may be an ephemeral feature in the permeability-controlled regime of the NW Caldera [39, 40]. During rock alteration and mineral precipitation in the subseafloor, fluid pathways may regularly open or close with this process controlling phase segregation, leading to alternating occurrences of vapor and brine over periods of days to months, instead of months to years for any chimney. The variability of our fluid inclusion data may be a product of both a temporal evolution of the site as a whole and a dynamic permeability regime in the subseafloor. Given the wide range of S_{eq} occurring in the fluid inclusions of most samples, we suggest the latter to be the dominant process.

5.3. Evidence from Isenthalpic-Isobaric Mixing Models. Isobaric-isenthalpic models of mixing between shallow (170 bar) phase-separated vapor-brine end-member pairs and ambient seawater can explain virtually the whole spectrum (92%) of our fluid inclusion data.

Five percent of all inclusions contain low-salinity fluids in combination with low T_e that fall below the temperature-salinity relation of the mixing line between phase-separated vapor and ambient seawater. These inclusions cannot be explained by mixing trends at seafloor pressures because fluids at lower temperatures do not phase separate at all. These inclusions can be interpreted as vapor end-member fluids that have conductively cooled prior to, or during, mixing with seawater. Alternatively, these inclusions may represent re-equilibrated inclusions that were originally produced by mixing of the pure vapor end-member with seawater, but which have since been offset to lower T_e values. Applying conductive cooling or re-equilibration for these inclusions does not contradict our proposed mixing model, and hence, 98% of the inclusions can be explained.

The remaining 2% of inclusions, not adequately explained by our model of subcritical phase separation, contain high-salinity brines (S_{eq} > 5 wt.% NaCl eq.) with low formation temperatures (<<300°C). Like the relatively low-T_e -low-S_{eq} inclusions, these brine inclusions may have been affected by conductive cooling or re-equilibration. Alternatively, these inclusions may have suffered from reaction between the fluid inclusions and their host crystal. For example, during microthermometric analysis, formation of gypsum after anhydrite on the inclusion walls may increase the salinity by up to ~50% from the original value [54]. However, a number of inclusions were measured to contain fluids with salinities of up to 18.6 wt.% NaCl eq., which cannot be produced by hydration of the host crystals with original salinities of <5.25 wt.% NaCl eq., as proposed for the subcritical region. Subcritical phase separation can account for such highly saline brines if a sufficient amount of vapor has fractionated off the hydrothermal fluid. For instance, a brine with 20 wt.% NaCl eq. can be produced if a mass fraction of 84 wt.% vapor fractionates off and separates from the remaining 16 wt.% brine. This fractionation would mean that the majority of fluids at the NW Caldera should represent vapor-derived fluids. This is clearly not the case considering the brine-dominated nature of the hydrothermal system as seen in the fluid inclusion data and the composition of vent fluids.

During microthermometric studies of fluid inclusions from IODP drillcore samples, S_{eq} of up to 45 wt.% NaCl eq. were measured [7]. These inclusions were considered to record a contribution of sequestered brines from near a magmatic-hydrothermal interface in the deeper parts of the hydrothermal system, originating from either supercritical phase separation or by the condensation of a single-phase magmatic fluid. Our second mixing model specifically calculates an isenthalpic-isobaric mixing path for a supercritically phase-separated brine-vapor pair formed at 340 bar. This model is consistent with supercritical phase separation accounting for the very high-salinity inclusions.

In summary, the rare high-salinity inclusions of up to 18.6 wt.% NaCl eq. are unlikely to be formed by crystals growing from fluids produced under shallow phase separation or conductive cooling conditions. Re-equilibration of the inclusions is also not considered a favorable mechanism to produce the low T_e values in these high S_{eq} inclusions but suggests that these inclusions are either a result of mixing between seawater and a deep-seated fluid produced by supercritical phase separation or condensation of a magmatic brine, as proposed by de Ronde et al. [7]. Our study shows that such a deep-seated brine may occasionally reach the shallowest part of the NW Caldera hydrothermal system and contributes to the composition of fluids that pass through stockwork zones to vent at the seafloor.

5.4. Seawater Entrainment and Sulfate Precipitation. We applied $^{87}Sr/^{86}Sr$ values to evaluate conductive heating/cooling and/or seawater mixing in the hydrothermal system,

similar to previous studies [8, 18, 19]. Values of $^{87}Sr/^{86}Sr$ in our sulfate separates (0.704852–0.709040) range from near hydrothermal end-member values of 0.70437 to seawater-like values of 0.70918 [47]. This range implies that the individual crystals/samples have precipitated from significantly different mixing regimes from largely hydrothermal fluids and seawater, as to be expected by mass balance equations. Multiple measurements of Sr isotopes for single samples in our study resulted in a considerable range of compositions (e.g., 085-6R1, $^{87}Sr/^{86}Sr = 0.704852$ to 0.706894) that require highly variable mixing on a temporal scale at one location.

In a setting where subcritical phase separation may produce vapors with very low salinities, using a mass balance approach with specific Sr contents for the hydrothermal end-member fluids may be problematic. The fluid inclusion data for individual samples (with a wide range in S_{eq}) shows that most crystals grew from vapor-derived fluids, as well as from brine-derived fluids. Vapor-derived fluids, assumed to be depleted in Sr, as well as all other major cations (according to the partitioning of salt) behave differently than seawater-like or brine-rich fluids. That is, Sr isotope mass balances show that such vapor-derived fluids, because of their very low Sr contents, will inherit a seawater isotope signature even after mixing with just a few weight percent of seawater. Consequently, crystals that grow from vapor-derived fluids that then mix with seawater will mimic seawater-derived $^{87}Sr/^{86}Sr$ signatures, although the hydrothermal component in a fluid-seawater mix may be dominating. The range of seawater-hydrothermal fluid mixing ratios derived from a simple Sr isotope mass balance may thus be overpredicted in systems in which phase separation plays an important role.

Considering the broad range in NW Caldera fluid inclusion S_{eq} within individual samples, we suggest that $^{87}Sr/^{86}Sr$ values for a single crystal, or even bulk samples, are controlled by what proportion of the crystal grew from brine-derived versus vapor-derived fluids, before mixing with seawater. This contrasts with the approach of using these values to determine hydrothermally dominated as opposed to seawater-dominated regimes. We therefore propose that much of the variation in NW Caldera $^{87}Sr/^{86}Sr$ values reflects the ephemeral character of phase segregation and the effects of vapor- and brine-derived fluids, rather than simple mixing between hydrothermal fluids and seawater.

For future investigations of this kind in relatively shallow island arc settings, we recommend conducting spatially resolved analytics of $^{87}Sr/^{86}Sr$ by laser-based methods to circumvent this problem and to determine if $^{87}Sr/^{86}Sr$ values are homogeneously distributed in individual crystals (cf. [8, 19]). In addition, to address the effect of hydrothermal fluid-seawater mixing versus vapor-brine contribution using Sr isotopes, $^{87}Sr/^{86}Sr$ values should also be evaluated in close relation with tracers of fluid salinities, or more specific, fluid Sr concentration.

We suggest that T_e provides a better proxy for any mixing regime for NW Caldera fluids. The temperature evolution is essentially the same for mixtures between brine- and vapor-derived fluids, and thus, temperature is not affected by phase separation, as are $^{87}Sr/^{86}Sr$ values. The problem of using temperature as a proxy for a mixing regime is still that temperature may be affected by conductive heating (or conductive cooling) without noticeably changing any chemical parameter in the fluid. Nevertheless, using temperature to evaluate the mixing regime would lead to conclude that the sulfates precipitated in dominantly hydrothermal conditions. Applying T_e values of inclusion samples to assess the mixing regime results in a hydrothermal component of between 0.5 and 0.9 (i.e., 50–90 wt.% hydrothermal fluid in the mixture) for all samples. By comparison, using individual inclusions results in a hydrothermal component between 0.35 and 0.95 (i.e., 35–95 wt.% hydrothermal fluid in the mixture).

In summary, the Sr data demonstrate that seawater entrainment was widespread and variable throughout the NW Caldera site, consistent with sulfate deposition in chimney walls and in the stockwork immediately below the vent field. This is consistent with other studies that demonstrate that sulfate precipitation as a consequence of mixing between hydrothermal fluids and seawater is commonplace in chimneys of the NW Caldera vent field [31, 41]. While the growth of sulfate crystals in mixing regimes with variable seawater contributions has been shown before in back-arc basins and mid-ocean ridges [8, 18, 19], this study demonstrates that these processes in shallow island arc systems with subcritical phase separation occurring at lower seafloor pressures are more complex.

6. Conclusions

High fluid inclusion entrapment temperatures (T_e) and a notable range in inclusion salinities (S_{eq}) in hydrothermal sulfate samples provide robust evidence for the ubiquitous nature of phase separation of hydrothermal fluids that formed chimneys and a mineralized stockwork zone at the Brothers NW Caldera vent field. If S_{eq} in fluid inclusions represent an integrated view of fluid salinities in a temporal and spatial fashion, more than half the fluids being expelled on the seafloor are brines (i.e., greater than seawater salinity), a third of the fluids are vapor derived (i.e., less than seawater salinity), with the remainder of seawater salinity. Only rare inclusions possibly represent supercritical phase separation or condensation of a magmatic brine.

Isobaric-isenthalpic mixing models of relatively shallow phase-separated fluids can explain the variability of 98% of all fluid inclusions in our study. They correctly predict the dominant occurrence of brines over vapors in the dataset. The mixing models suggest that the majority of fluids are phase separating in only 10 s to few 100 s mbsf (at a pressure of ~170 bar). Mixing with cold seawater occurs during the very final stage of ascent of these fluids.

A new discovery of this study is that high T_e (up to the depth-to-boiling-point curve) at seafloor pressures and extremely low salinities (down to 0.1 wt.% NaCl eq., in fluid inclusions) in the NW Caldera site are also consistent with phase-separating fluids having sporadically reached the seafloor.

Rare, high-salinity fluid inclusions (>5.25 to 18.6 wt.% NaCl eq.) and possibly halite-bearing three-phased inclusions are unlikely produced by shallow phase separation. These inclusions are thought to represent periodic injection

of deep-seated brines into the shallower part of the hydrothermal system. This finding corroborates results from microthermometric studies in IODP drillcore samples and shows that deep-seated brines can be transported to the seafloor and may play a role in the mineralization of chimneys and stockwork mineralization, consistent with the findings of Berkenbosch et al. [42, 66] who used Cu isotopes and trace element mapping to show how some of the mineralization has a magmatic affinity.

Since phase-separation processes are shown to produce salt-poor vapors that result in seawater-type isotope signatures, $^{87}Sr/^{86}Sr$ mass balance calculations used to evaluate mixing regimes in shallow arc environments should be used with caution. We suggest that the application of Sr isotopes should be used with spatially resolvable methods and in close conjunction with the evaluation of Sr concentration of the mineralizing hydrothermal fluids. Based on fluid inclusion entrapment temperatures, our mixing models suggest that mineralization in the NW Caldera is occurring in a hydrothermally dominated mixing regime with less than 50% of seawater.

Data Availability

The datasets associated with this article are accessible via the information system PANGAEA (https://doi.org/10.1594/PANGAEA.920208). The datasets contain the fluid inclusion raw data (https://doi.pangaea.de/10.1594/PANGAEA.920191) and the $^{87}Sr/^{86}Sr$ values (https://doi.pangaea.de/10.1594/PANGAEA.920192).

Conflicts of Interest

The authors declare that there is no conflict of interest regarding the publication of this paper.

Acknowledgments

The research cruise TN350 was supported by the U.S. National Science Foundation awards (OCE-1558356) to Susan Humphris and (OCE-1558795) to Anna-Louise Reysenbach. Interridge is thanked for a travel fund that enabled A.D. to participate on cruise TN350. The Bundesministerium für Bildung und Forschung (BMBF) provided funding for cruise SO253 and this work with grant no. 03G0253B. A.D. was also partly supported by the MARUM Center for Marine Environmental Science. We acknowledge the science teams, crews, and captains of the R/V *Sonne* and R/V *Thompson* for their work. Thanks are due to the teams of ROV *QUEST* and *Jason II* for their efforts to recover rock specimens that made this study possible. Special thanks goes to Andreas Klügel for instructions in the use of the microthermometry stage, to Friedrich Lucassen for his support during lab work and TIMS analysis, Janis Thal for providing gridded multibeam data acquired during cruise SO253, and Patrick Monien for proofreading und useful comments in the early stage of this manuscript. We acknowledge the two anonymous reviewers for their useful comments that improved the overall quality of the manuscript.

References

[1] T. H. Hansteen and A. Klügel, "Fluid inclusion thermobarometry as a tracer for magmatic processes," *Reviews in Mineralogy and Geochemistry*, vol. 69, no. 1, pp. 143–177, 2008.

[2] M. A. Longpre, A. Klügel, A. Diehl, and J. Stix, "Mixing in mantle magma reservoirs prior to and during the 2011-2012 eruption at El Hierro, Canary Islands," *Geology*, vol. 42, no. 4, pp. 315–318, 2014.

[3] B. Bieseler, A. Diehl, N. Jöns, F. Lucassen, and W. Bach, "Constraints on cooling of the lower ocean crust from Epidote veins in the Wadi Gideah section, Oman Ophiolite," *Geochemistry, Geophysics, Geosystems*, vol. 19, no. 11, pp. 1–23, 2018.

[4] R. J. Bodnar, P. Lecumberri-Sanchez, D. Moncada, and M. Steele-MacInnis, "Fluid inclusions in hydrothermal ore deposits," *Treatise on Geochemistry*, vol. 13, pp. 119–142, 2014.

[5] M. O. Anderson, M. D. Hannington, T. F. McConachy et al., "Mineralization and alteration of a modern seafloor massive sulfide deposit hosted in mafic volcaniclastic rocks," *Economic Geology*, vol. 114, no. 5, pp. 857–896, 2019.

[6] C. E. de Ronde, K. Faure, C. J. Bray, D. A. Chappell, and I. C. Wright, "Hydrothermal fluids associated with seafloor mineralization at two southern Kermadec arc volcanoes, offshore New Zealand," *Mineralium Deposita*, vol. 38, no. 2, pp. 217–233, 2003.

[7] C. E. J. de Ronde, S. E. Humphris, T. W. Höfig, A. G. Reyes, and the IODP Expedition 376 Scientists, "Critical role of caldera collapse in the formation of seafloor mineralization: the case of Brothers volcano," *Geology*, vol. 47, no. 8, pp. 762–766, 2019.

[8] J. W. Jamieson, M. D. Hannington, M. K. Tivey et al., "Precipitation and growth of barite within hydrothermal vent deposits from the Endeavour Segment, Juan de Fuca Ridge," *Geochimica et Cosmochimica Acta*, vol. 173, pp. 64–85, 2016.

[9] D. S. Kelley and J. R. Delaney, "Two-phase separation and fracturing in mid-ocean ridge gabbros at temperatures greater than 700 °C," *Earth and Planetary Science Letters*, vol. 83, pp. 53–66, 1987.

[10] C. Lécuyer, M. Dubois, C. Marignac, G. Gruau, Y. Fouquet, and C. Ramboz, "Phase separation and fluid mixing in subseafloor back arc hydrothermal systems: a microthermometric and oxygen isotope study of fluid inclusions in the barite-sulfide chimneys of the Lau Basin," *Journal of Geophysical Research: Solid Earth*, vol. 104, no. B8, pp. 17911–17927, 1999.

[11] J. M. Peter and S. D. Scott, "Mineralogy, composition, and fluid-inclusion microthermometry of seafloor hydrothermal deposits in the southern through of Guaymas basin, gulf of California," *Canadian Mineralogist*, vol. 26, pp. 567–587, 1988.

[12] D. A. Vanko, W. Bach, S. Roberts, C. J. Yeats, and S. D. Scott, "Fluid inclusion evidence for subsurface phase separation and variable fluid mixing regimes beneath the deep-sea PACMANUS hydrothermal field, Manus Basin back arc rift, Papua New Guinea," *Journal of Geophysical Research*, vol. 109, no. B3, 2004.

[13] A. B. Atkinson Jr., *A Model for the PTX Properties of H_2O-NaCl*, State University, Blacksburg, Virginia, 2002.

[14] R. J. Bodnar and M. O. Vityk, "Interpretation of microthermometric data for H_2O-NaCl fluid inclusions," in *Fluid Inclusions in Minerals, Methods and Applications*, B. Vivo and M. L. Frezzotti, Eds., pp. 117–130, Virginia Tech, Blacksburg, VA, 1994.

[15] R. J. Bodnar, "Reequilibration of fluid inclusions," in *Fluid Inclusions: Analysis and Interpretation*, I. Samson, A. Anderson, and D. Marshall, Eds., pp. 213–230, Mineral, Assoc. Canada, 2003.

[16] T. Baker and J. Lang, "Fluid inclusion characteristics of intrusion-related gold mineralization, Tombstone-Tungsten magmatic belt, Yukon Territory, Canada," *Mineralium Deposita*, vol. 36, no. 6, pp. 563–582, 2001.

[17] G. Xu, "Fluid inclusions with NaCl–$CaCl2_2$–$H2O_2$ composition from the Cloncurry hydrothermal system, NW Queensland, Australia," *Lithos*, vol. 53, no. 1, pp. 21–35, 2000.

[18] S. E. Humphris and W. Bach, "On the Sr isotope and REE compositions of anhydrites from the TAG seafloor hydrothermal system," *Geochimica et Cosmochimica Acta*, vol. 69, no. 6, pp. 1511–1525, 2005.

[19] P. R. Craddock and W. Bach, "Insights to magmatic–hydrothermal processes in the Manus back-arc basin as recorded by anhydrite," *Geochimica et Cosmochimica Acta*, vol. 74, no. 19, pp. 5514–5536, 2010.

[20] I. H. Widanagamage, *Stable strontium isotope fractionation in abiotic and microbially mediated barite in modern continental settings.*, Kent State University, 2015.

[21] R. W. Embley, C. E. J. de Ronde, S. G. Merle, B. Davy, and F. C. Tontini, "Detailed morphology and structure of an active submarine arc caldera: Brothers volcano, Kermadec arc," *Economic Geology*, vol. 107, no. 8, pp. 1557–1570, 2012.

[22] I. C. Wright and J. A. Gamble, "Southern Kermadec submarine caldera arc volcanoes (SW Pacific): caldera formation by effusive and pyroclastic eruption," *Marine Geology*, vol. 161, no. 2-4, pp. 207–227, 1999.

[23] K. M. Haase, N. Stroncik, D. Garbe-Schönberg, and P. Stoffers, "Formation of island arc dacite magmas by extreme crystal fractionation: an example from Brothers seamount, Kermadec island arc (SW Pacific)," *Journal of Volcanology and Geothermal Research*, vol. 152, no. 3-4, pp. 316–330, 2006.

[24] K. M. Haase, T. J. Worthington, P. Stoffers, D. Garbe-Schönberg, and I. Wright, "Mantle dynamics, element recycling, and magma genesis beneath the Kermadec Arc-Havre Trough," *Geochemistry, Geophysics, Geosystems*, vol. 3, no. 11, pp. 1–22, 2002.

[25] M. Keith, K. M. Haase, R. Klemd, D. J. Smith, U. Schwarz-Schampera, and W. Bach, "Constraints on the source of Cu in a submarine magmatic-hydrothermal system, Brothers volcano, Kermadec island arc," *Contributions to Mineralogy and Petrology*, vol. 173, no. 5, 2018.

[26] C. Timm, C. E. J. de Ronde, M. I. Leybourne, D. Layton-Matthews, and I. J. Graham, "Sources of chalcophile and siderophile elements in Kermadec Arc lavas," *Economic Geology*, vol. 107, no. 8, pp. 1527–1538, 2012.

[27] I. E. M. Smith, T. J. Worthington, R. B. Stewart, R. C. Price, and J. A. Gamble, "Felsic volcanism in the Kermadec arc, SW Pacific: crustal recycling in an oceanic setting," *Geological Society, London, Special Publications*, vol. 219, no. 1, pp. 99–118, 2003.

[28] E. T. Baker, S. L. Walker, R. W. Embley, and C. E. J. de Ronde, "High-resolution hydrothermal mapping of Brothers Caldera, Kermadec Arc," *Economic Geology*, vol. 107, no. 8, pp. 1583–1593, 2012.

[29] F. Caratori Tontini, B. Davy, C. E. J. de Ronde, R. W. Embley, M. Leybourne, and M. A. Tivey, "Crustal magnetization of Brothers volcano, New Zealand, measured by autonomous underwater vehicles: geophysical expression of a submarine hydrothermal system," *Economic Geology*, vol. 107, no. 8, pp. 1571–1581, 2012.

[30] C. E. J. de Ronde, E. T. Baker, G. J. Massoth et al., "Intra-oceanic subduction-related hydrothermal venting, Kermadec volcanic arc, New Zealand," *Earth and Planetary Science Letters*, vol. 193, no. 3-4, pp. 359–369, 2001.

[31] C. E. J. de Ronde, M. D. Hannington, P. Stoffers et al., "Evolution of a submarine magmatic-hydrothermal system: Brothers volcano, southern Kermadec arc, New Zealand," *Economic Geology*, vol. 100, no. 6, pp. 1097–1133, 2006.

[32] G. J. Massoth, C. E. De Ronde, J. E. Lupton et al., "Chemically rich and diverse submarine hydrothermal plumes of the southern Kermadec volcanic arc (New Zealand)," in *Intra-Oceanic Subduction Systems: Tectonic and Magmatic Processes*, R. D. Larter and P. T. Leat, Eds., pp. 119–139, Geological Society, London, 2003.

[33] C. E. J. de Ronde, G. J. Massoth, D. A. Butterfield et al., "Submarine hydrothermal activity and gold-rich mineralization at Brothers Volcano, Kermadec Arc, New Zealand," *Mineralium Deposita*, vol. 46, no. 5-6, pp. 541–584, 2011.

[34] F. Caratori Tontini, C. E. J. de Ronde, D. Yoerger, J. Kinsey, and M. Tivey, "3-D focused inversion of near-seafloor magnetic data with application to the Brothers volcano hydrothermal system, Southern Pacific Ocean, New Zealand," *Journal of Geophysical Research: Solid Earth*, vol. 117, no. B10, 2012.

[35] F. Caratori Tontini, M. A. Tivey, C. E. J. Ronde, and S. E. Humphris, "Heat flow and near-seafloor magnetic anomalies highlight hydrothermal circulation at Brothers Volcano Caldera, Southern Kermadec Arc, New Zealand," *Geophysical Research Letters*, vol. 46, no. 14, pp. 8252–8260, 2019.

[36] C. E. J. de Ronde, "Fluid chemistry and isotopic characteristics of seafloor hydrothermal systems and associated VMS deposits: potential for magmatic contributions," in *Magmas, Fluids, and Ore Deposits*, Short course handbook/Mineralogical Association of Canada 23, J. F. H. Thompson, Ed., pp. 479–521, Mineralogical Association of Canada, Victoria, BC, 1995.

[37] C. E. J. de Ronde and V. K. Stucker, "Chapter 47 - Seafloor Hydrothermal Venting at Volcanic Arcs and Backarcs," in *The Encyclopedia of Volcanoes*, pp. 823–849, Elsevier B.V., 2015.

[38] R. P. Dziak, J. H. Haxel, H. Matsumoto et al., "Observations of regional seismicity and local harmonic tremor at Brothers volcano, south Kermadec arc, using an ocean bottom hydrophone array," *Journal of Geophysical Research: Solid Earth*, vol. 113, no. B8, 2008.

[39] G. Gruen, P. Weis, T. Driesner, C. E. J. de Ronde, and C. A. Heinrich, "Fluid-flow patterns at Brothers Volcano, Southern Kermadec Arc: insights from geologically constrained numerical simulations," *Economic Geology*, vol. 107, no. 8, pp. 1595–1611, 2012.

[40] G. Gruen, P. Weis, T. Driesner, C. A. Heinrich, and C. E. J. de Ronde, "Hydrodynamic modeling of magmatic–hydrothermal activity at submarine arc volcanoes, with implications for ore formation," *Earth and Planetary Science Letters*, vol. 404, pp. 307–318, 2014.

[41] H. A. Berkenbosch, C. E. J. de Ronde, J. B. Gemmell, A. W. McNeill, and K. Goemann, "Mineralogy and formation of black smoker chimneys from Brothers Submarine Volcano, Kermadec Arc," *Economic Geology*, vol. 107, no. 8, pp. 1613–1633, 2012.

[42] H. A. Berkenbosch, C. E. J. de Ronde, B. T. Paul, and J. B. Gemmell, "Characteristics of Cu isotopes from chalcopyrite-rich black smoker chimneys at Brothers volcano, Kermadec arc, and Niuatahi volcano, Lau basin," *Mineralium Deposita*, vol. 50, no. 7, pp. 811–824, 2015.

[43] I. C. Wright, C. E. J. de Ronde, K. Faure, and J. A. Gamble, "Discovery of hydrothermal sulfide mineralization from southern Kermadec arc volcanoes (SW Pacific)," *Earth and Planetary Science Letters*, vol. 164, no. 1-2, pp. 335–343, 1998.

[44] C. E. J. de Ronde, S. E. Humphris, T. W. Höfig et al., "Expedition 376 methods," *Proceedings of the International Ocean Discovery Program*, vol. 376, 2019.

[45] P. Bird, "An updated digital model of plate boundaries," *Geochemistry, Geophysics, Geosystems*, vol. 4, no. 3, 2003.

[46] C. DeMets, R. G. Gordon, and D. F. Argus, "Geologically current plate motions," *Geophysical Journal International*, vol. 181, no. 1, pp. 1–80, 2010.

[47] A. Diehl, *Causes for variable hydrothermal vent fluid compositions in intraoceanic arcs - insights from fluid compositions and mineral precipitates of the South Kermadec Arc*, University Bremen, Bremen, 2019.

[48] C. Kleint, W. Bach, A. Diehl et al., "Geochemical characterization of highly diverse hydrothermal fluids from volcanic vent systems of the Kermadec intraoceanic arc," *Chemical Geology*, vol. 528, no. 119289, pp. 1–20, 2019.

[49] S. E. Humphris, A.-L. Reysenbach, and M. Tivey, *Brothers Volcano March 6-26, 2018 R/V Thomas Thompson, ROV Jason TN350 Cruise Report*, Woods Hole Oceanographic Institution, 2018.

[50] A. Koschinsky, *RV Sonne 253 Cruise Report/Fahrtbericht, Nouméa (New Caledonia) 22.12.2016 - Auckland (New Zealand) 21.01.2017, SO253 - HYDROTHERMADEC*, Jacobs University Bremen, Bremen, 2017.

[51] A. Koschinsky, J. Thal, and A.-C. Wölfl, *Raw multibeam EM122 data: transits of SONNE cruise SO253 (South Pacific)*, PANGAEA, 2018.

[52] R. J. Bodnar, "Introduction to fluid inclusions," in *Fluid Inclusions: Analysis and Interpretation*, I. Samson, A. Anderson, and D. Marshall, Eds., pp. 1–8, Mineral, Assoc. Canada, 2003.

[53] E. Roedder, "The origin of fluid inclusions," in *Fluid inclusions*, P. H. Ribbe, Ed., pp. 11–46, Mineralogical Society of America, 1984.

[54] D. A. Vanko and W. Bach, "Heating and freezing experiments on aqueous fluid inclusions in anhydrite: recognition and effects of stretching and the low-temperature formation of gypsum," *Chemical Geology*, vol. 223, no. 1-3, pp. 35–45, 2005.

[55] C. Deniel and C. Pin, "Single-stage method for the simultaneous isolation of lead and strontium from silicate samples for isotopic measurements," *Analytica Chimica Acta*, vol. 426, no. 1, pp. 95–103, 2001.

[56] K. P. Jochum, U. Nohl, K. Herwig, E. Lammel, B. Stoll, and A. W. Hofmann, "GeoReM: a new geochemical database for reference materials and isotopic standards," *Geostandards and Geoanalytical Research*, vol. 29, no. 3, pp. 333–338, 2005.

[57] T. Driesner and C. A. Heinrich, "The system H_2O–NaCl. Part I: correlation formulae for phase relations in temperature–pressure–composition space from 0 to 1000°C, 0 to 5000bar, and 0 to 1 X_{NaCl}," *Geochimica et Cosmochimica Acta*, vol. 71, no. 20, pp. 4880–4901, 2007.

[58] T. Driesner, "The system H_2O–NaCl. Part II: correlations for molar volume, enthalpy, and isobaric heat capacity from 0 to 1000°C, 1 to 5000bar, and 0 to 1 X_{NaCl}," *Geochimica et Cosmochimica Acta*, vol. 71, no. 20, pp. 4902–4919, 2007.

[59] L. Haar, J. S. Gallagher, and G. S. Kell, *NBS/NRC Steam Tables: Thermodynamic and Transport Properties and Computer Programs for Vapor and Liquid States of Water in SI Units*, Hemisphere Publishing Corporation, 1984.

[60] E. T. Baker, "Characteristics of hydrothermal discharge following a magmatic intrusion," *Geological Society, London, Special Publications*, vol. 87, no. 1, pp. 65–76, 1995.

[61] D. A. Butterfield, K. K. Roe, M. D. Lilley et al., "Mixing, reaction and microbial activity in the sub-seafloor revealed by temporal and spatial variation in diffuse flow vents at axial volcano," *The Subseafloor Biosphere at Mid-Ocean Ridges*, vol. 144, pp. 269–289, 2004.

[62] D. j. Fornari, K. L. von Damm, J. G. Bryce et al., "The East Pacific rise between 9°N and 10°N: twenty-five years of integrated, multidisciplinary oceanic spreading center studies," *Oceanography*, vol. 25, no. 1, pp. 18–43, 2012.

[63] R. G. Ditchburn and C. E. J. de Ronde, "Evidence for remobilization of barite affecting radiometric dating using ^{228}Ra, $_{228}$Th, and ^{226}Ra/Ba values: implications for the evolution of sea-floor volcanogenic massive sulfides," *Economic Geology*, vol. 112, no. 5, pp. 1231–1245, 2017.

[64] R. G. Ditchburn, C. E. J. de Ronde, and B. J. Barry, "Radiometric dating of volcanogenic massive sulfides and associated Iron oxide crusts with an emphasis on ^{226}Ra/Ba and $_{228}$Ra/^{226}Ra in volcanic and hydrothermal processes at intraoceanic arcs," *Economic Geology*, vol. 107, no. 8, pp. 1635–1648, 2012.

[65] D. A. Butterfield, G. J. Massoth, R. E. McDuff, J. E. Lupton, and M. D. Lilley, "Geochemistry of hydrothermal fluids from axial seamount hydrothermal emissions study vent field, Juan de Fuca Ridge: subseafloor boiling and subsequent fluid-rock interaction," *Journal of Geophysical Research*, vol. 95, no. B8, pp. 12895–12921, 1990.

[66] H. A. Berkenbosch, C. E. J. de Ronde, C. G. Ryan et al., "Trace element mapping of copper- and zinc-rich black smoker chimneys from Brothers Volcano, Kermadec Arc, using synchrotron radiation XFM and LA-ICP-MS," *Economic Geology*, vol. 114, no. 1, pp. 67–92, 2019.